minerals

MDPI

Article

Isomorphism and Mutual Transformations of S-Bearing Components in Feldspathoids with Microporous Structures

Nikita V. Chukanov [1,2,*], Nadezhda V. Shchipalkina [2], Roman Yu. Shendrik [2,3], Marina F. Vigasina [2], Vladimir L. Tauson [3], Sergey V. Lipko [3], Dmitry A. Varlamov [1,4], Vasiliy D. Shcherbakov [2], Anatoly N. Sapozhnikov [3], Anatoly V. Kasatkin [5], Natalia V. Zubkova [2] and Igor V. Pekov [2,6]

[1] Institute of Problems of Chemical Physics, Russian Academy of Sciences, 142432 Chernogolovka, Russia
[2] Faculty of Geology, Moscow State University, 119991 Moscow, Russia
[3] Vinogradov Institute of Geochemistry, Siberian Branch of Russian Academy of Sciences, 664033 Irkutsk, Russia
[4] Institute of Experimental Mineralogy RAS, 142432 Chernogolovka, Russia
[5] Fersman Mineralogical Museum of the Russian Academy of Sciences, 119071 Moscow, Russia
[6] Vernadsky Institute of Geochemistry and Analytical Chemistry, Russian Academy of Sciences, 119991 Moscow, Russia
* Correspondence: chukanov@icp.ac.ru

Abstract: The isomorphism of S-bearing feldspathoids belonging to the cancrinite, sodalite, tugtupite, vladimirivanovite, bystrite, marinellite and scapolite structure types has been investigated using a multimethodical approach based on infrared, Raman and electron spin resonance (ESR), as well as ultraviolet, visible and near infrared (UV–Vis–near IR) absorption spectroscopy methods and involving chemical and X-ray diffraction data. Sapozhnikovite $Na_8(Al_6Si_6O_{24})(HS)_2$ and sulfite and thiosulfate analogues of cancrinite are synthesized hydrothermally and characterized by means of electron microprobe analyses, powder X-ray diffraction and Raman spectroscopy. The possibility of the incorporation of significant amounts of SO_4^{2-}, S_4 and SO_3^{2-} in the crystal structures of cancrisilite, sulfhydrylbystrite and marinellite, respectively, has been established for the first time. Thermal conversions of S-bearing groups in the synthetic sulfite cancrinite and sapozhnikovite analogues as well as natural vladinirivanovite and S_4-bearing haüyne under oxidizing and reducing conditions have been studied using the multimethodical approach. The SO_4^{2-} and S^{2-} anions and the $S_3^{\bullet-}$ radical anion are the most stable S-bearing species under high-temperature conditions (in the range of 700–800 °C); their ratio in the heated samples is determined by the redox conditions and charge-balance requirement. The HS^- and S_5^{2-} anions are stable only under highly reducing conditions.

Keywords: feldspathoids; isomorphism; solid solutions; sulfur; infrared spectroscopy; electron spectroscopy; Raman spectroscopy; electron spin resonance; photoluminescence

Citation: Chukanov, N.V.; Shchipalkina, N.V.; Shendrik, R. Y.; Vigasina, M.F.; Tauson, V.L.; Lipko, S.V.; Varlamov, D.A.; Shcherbakov, V.D.; Sapozhnikov, A.N.; Kasatkin, A.V.; et al. Isomorphism and Mutual Transformations of S-Bearing Components in Feldspathoids with Microporous Structures. *Minerals* **2022**, *12*, 1456. https://doi.org/10.3390/min12111456

Academic Editor: Luca Bindi

Received: 20 October 2022
Accepted: 15 November 2022
Published: 18 November 2022

1. Introduction

Feldspathoids are defined as framework aluminosilicates (tectosilicates) which are anhydrous (leucite and nepheline-group minerals) or contain extra-framework anions (microporous aluminosilicates belonging to the sodalite, cancrinite and scapolite groups) [1,2]. Some feldspathoids are among the main components of different kinds of magmatic and metasomatic rocks. The extra-framework components in feldspathoids which have microporous structures are very diverse and include alkali and alkaline–earth cations (mainly, Na^+, K^+ and Ca^{2+}), anions (SO_4^{2-}, SO_3^{2-}, PO_4^{3-}, CO_3^{2-}, $C_2O_4^{2-}$, Cl^-, HS^-, OH^-, F^- and S_n^{2-} with n from 1 to 5, MoO_4^{2-}, WO_4^{2-}, AsO_4^{3-}, etc.), radical anions ($S_2^{\bullet-}$, $S_3^{\bullet-}$, *cis*- and *trans*-$S_4^{\bullet-}$, $SO_4^{\bullet-}$) and neutral molecules (H_2O, CO_2, COS, *cis*- and *trans*-S_4, S_6, etc.) [3–14] (the components playing a species-defining role in some minerals are given in bold type;

"•" means an unpaired electron).

The extra-framework components in feldspathoids are important markers of redox conditions and fugacities of volatile components during the formation of rock [6,13,15,16]. On the other hand, the microporous compounds belonging to the topological types of sodalite and, to a less extent, cancrinite are considered to be advanced materials that can be used in different technologies [4,17–46].

As one can see from the above list of extra-framework components in feldspathoids, S-bearing species are most diverse: the oxidation degree of sulfur, the polymerization degree of sulfide sulfur and the charge of S-bearing species in feltspathoids varies from 0 to 6, from 1 to 6 and from 0 to −2, respectively. To date, a theoretical and methodological basis has been created for the study of various forms of sulfur and the mechanisms of their mutual transformations [4–6,8,12,13,47–63]. In this paper, we provide new data on the formation, isomorphism and mutual conversions of S-bearing extra-framework components in some feldspathoids and their synthetic counterparts.

2. Materials and Methods

2.1. Natural Samples

The studied samples are listed below. Their empirical formulae are partly taken from literature sources. Chemical data for the newly analyzed samples of feldspathoids are given in Tables 1–3. For samples with unknown contents of CO_3^{2-} and unknown ratios of different S-bearing species, these values were calculated based on the charge-balance requirement. All anionic groups and neutral molecules in the empirical formulae are confirmed by structural data or by using spectroscopic methods.

Sample 1 is cancrinite from the Mica mine, Kovdor alkaline complex, Kola Peninsula, Russia. Its empirical formula is [12]: $Na_{6.7}Ca_{0.7}(Si_{6.5}Al_{5.5}O_{24})(CO_3)_{1.3}\cdot nH_2O$ (Z = 1). The mineral forms grey short-prismatic crystals up to 3 cm long in association with pectolite, potassic feldspar and aegirine-diopside.

Sample 2 is a CO_3^{2-}-bearing variety of vishnevite from Loch Borrolan, Scotland, GB [64]. Its empirical formula is $Na_{6.46}Ca_{0.88}K_{0.08}(Si_{6.18}Al_{5.82}O_{24})(SO_4)_{0.74}(CO_3)_{0.50}\cdot nH_2O$ (Z = 1).

Sample 3 is lilac S- and P-bearing cancrisilite from Alluaiv Mt., Lovozero massif, Kola Peninsula, Russia. The sample originates from a peralkaline pegmatite and associates with HS^--bearing sodalite. Its chemical composition is given in Table 1. The empirical formula of Sample 3 is $Na_{7.45}K_{0.03}(Si_{6.84}Al_{5.10}Fe^{3+}_{0.05}O_{24})(CO_3)_{0.775}(SO_4)_{0.32}(PO_4)_{0.05}Cl_{0.04}\cdot nH_2O$ (the content of the carbonate groups was calculated from the charge balance requirement).

Sample 4 is a common lilac S-free cancrisilite sample from Alluaiv Mt. Its empirical formula is $Na_{7.17}(Si_{7.39}Al_{4.61}O_{24})(CO_3)_{1.28}\cdot nH_2O$ [64].

Sample 5 is bright blue S_4-bearing haüyne with the empirical formula $Na_{6.45}K_{0.01}Ca_{1.36}(Si_{6.06}Al_{5.94}O_{24})(SO_4)_{1.56}(S_4)_{0.09}(S_3^{\bullet-})_{0.03}Cl_{0.09}(CO_2)_{0.02}\cdot nH_2O$ [5,13]. The unit cell parameter is a = 9.071 Å. The mineral forms grains in coarse-grained calciphyre consisting mainly of calcite, with subordinate diopside, scapolite and relics of plagyoclase. Sample 5 has been collected at the Pokhabinskoe lapis lazuli deposit situated in the basin of the Pokhabikha river, Slyudyanka district, Irkutsk region, Baikal Lake area, Siberia, Russia. A 30 cm thick tectonic zone of fractured metasomatic rocks with sodalite-group minerals occurs there at the contact of marbles and igneous rocks (leucomonzonites and anorthosites).

Sample 6 is the neotype specimen of lazurite with the empirical formula $(Na_{6.97}Ca_{0.88}K_{0.10})(Si_{6.04}Al_{5.96}O_{24})(SO_4)_{1.09}(S_3^{\bullet-})_{0.55}S^{2-}_{0.05}Cl_{0.04}\cdot 0.72H_2O$ from the Malo-Bystrinskoe gem lazurite deposit, Baikal Lake area, Siberia, Russia. [6]. The associated minerals are calcite and diopside as well as accessory dolomite, forsterite and phlogopite. The crystal structure of Sample 6 is characterized by commensurate and incommensurate modulations; the a parameter of the cubic sub-cell is equal to 9.087(3) Å.

Table 1. Chemical composition (wt.%) of S- and P-bearing cancrisilite (Sample 3).

Component	Spot Analysis No.				Mean
	1	2	3	4	
Na_2O	23.02	22.60	22.78	22.69	22.77
K_2O	0.18	0.16	0.15	0.10	0.15
Al_2O_3	25.85	25.23	25.80	25.64	25.63
Fe_2O_3	0.72	0.52	0.38	0.35	0.49
SiO_2	39.66	41.34	40.40	40.82	40.56
P_2O_5	0.24	0.42	0.45	0.26	0.34
SO_3	2.27	2.23	2.87	2.67	2.51
Cl	0.22	0.11	0.14	0.09	0.14
$-O\equiv Cl$	−0.05	−0.02	−0.03	−0.02	−0.03
Total	92.11	92.59	92.94	92.60	92.56

Sample 7 is the holotype specimen of vladimirivanovite, an orthorhombic (space group *Pnaa*) lazurite-related mineral from the Tultui gem lazurite deposit, Baikal Lake area, Siberia, Russia [65]. The mineral forms dark blue zones around lazurite grains and separate elongate individuals up to 4 mm long. The other associated minerals are calcite, afghanite, tounkite, phlogopite and marialite. The Raman spectrum of Sample 7 shows the presence of significant amounts of the $S_3^{\bullet-}$ radical anions. The charge-balanced empirical formula written under the assumption that all sulfide sulfur belongs to $S_3^{\bullet-}$ is $(Na_{6.36}Ca_{1.52})(Si_{6.03}Al_{5.97}O_{24})(SO_4)_{1.08}(S_3^{\bullet-})_{0.22}Cl_{0.04}\cdot 0.62H_2O$.

Sample 8 is tugtupite, $Na_8(Si_8Al_2Be_2O_{24})Cl_2$, originating from its type locality, Tugtup Agtakorfia, Ilimaussaq alkaline complex, Greenland. The mineral forms rose-colored equant grains up to 1 cm across in peralkaline pegmatite. Tugtupite is not considered as a feldspathoid, but it belongs to the sodalite group and was studied in this work for a comparison.

Sample 9 is bystrite from the Malo-Bystrinskoe gem lazurite deposit. The mineral forms yellow anhedral equant grains up to 0.5 mm across in partly recrystallized lazurite calciphyre. The associated minerals are calcite, lazurite, sodalite, fluorapatite, phlogopite, diopside and dolomite (Figures 1 and 2a). Bystrite grains are embedded in calcite granular aggregate. Lazurite and bystrite do not show any reaction relations. Sodalite forms inclusions in bystrite and lazurite, and dolomite occurs as inclusions in calcite. Locally, bystrite occurs as a component of fine-grained polymineral aggregates, in which grains of earlier minerals are partly substituted with phlogopite (Figure 2b). The chemical composition of Sample 9 is given in Table 2. The empirical formula of Sample 9 is $Na_{6.75}K_{0.04}Ca_{1.11}(Si_{6.09}Al_{5.91}O_{24})(S_5)^{2-}{}_{1.04}(HS^-)_{0.17}Cl_{0.85}\cdot nH_2O$ ($Z = 2$; sulfur is divided among S_5^{2-} and HS^-, taking into account the charge-balance requirement). The presence of HS^- in this sample is confirmed by the Raman spectrum (see below).

Sample 10 is orange–yellow bystrite from the Malo-Bystrinskoe gem lazurite deposit. Its chemical composition is (wt.%): Na_2O 19.51, K_2O 0.16, CaO 4.97, Al_2O_3 27.61, SiO_2 32.72, S_5^{2-} 13.46, SO_3 1.08, Cl^- 2.66, $-O=(Cl^-, S_5^{2-})$ −1.94, total 100.23 (sulfur is divided among S_5^{2-} and SO_3, taking into account the charge-balance requirement). The presence of a minor amount of sulfate sulfur in Sample 10 is confirmed by Raman spectroscopy. The empirical formula of Sample 10 is $Na_{6.97}K_{0.04}Ca_{0.98}(Si_{6.03}Al_{5.97}O_{24})(S_5^{2-})_{0.93}(SO_4^{2-})_{0.15}Cl_{0.83}$ ($Z = 2$).

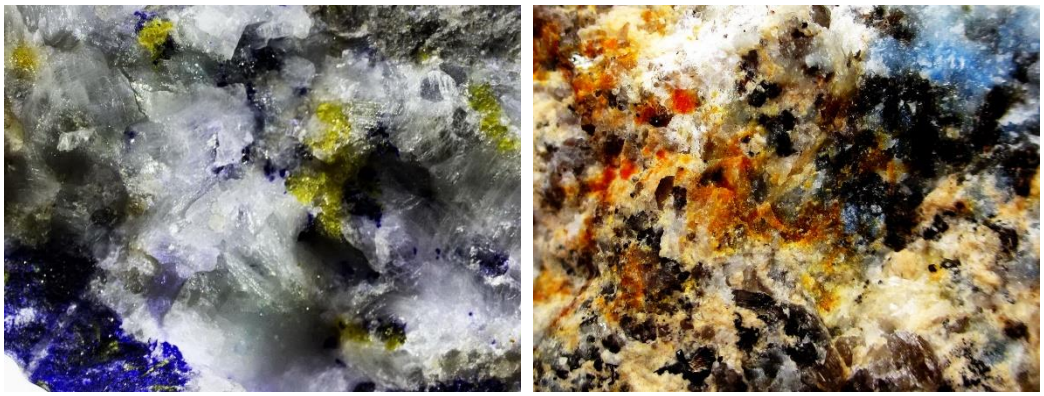

(**a**) (**b**)

Figure 1. Grains of (**a**) bystrite (Sample 9, yellow) in association with lazurite (deep blue) and calcite (white) and (**b**) sulfhydrylbystrite (red–orange) in association with afghanite (pale blue), diopside (dark grayish green to almost black), nepheline (grey), plagioclase (yellowish to beige) and calcite (white). The field of view (FOV) widths are (**a**) 16 mm and (**b**) 20 mm.

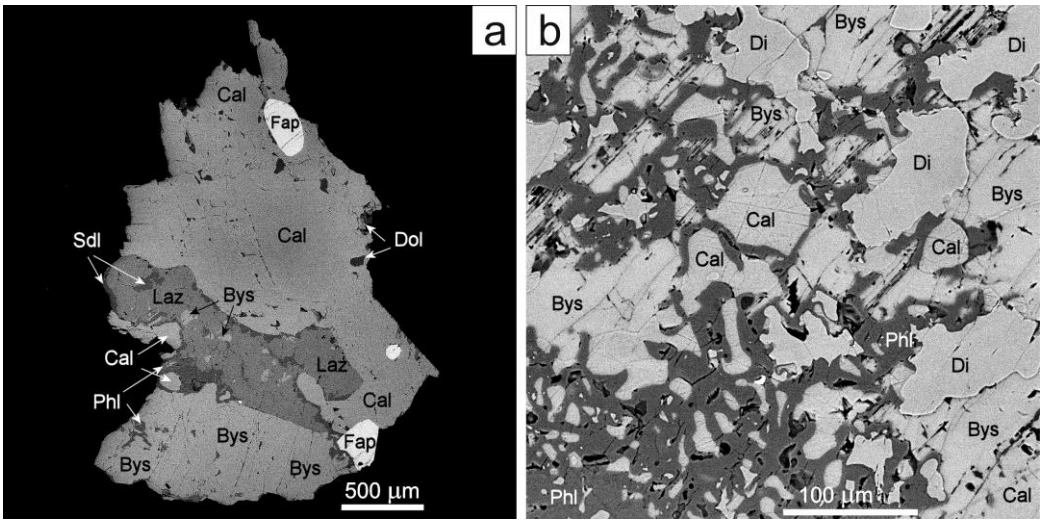

Figure 2. Mineral associations of bystrite (Bys, Sample 9) with lazurite (Laz), sodalite (Sdl), calcite (Cal), dolomite (Dol), fluorapatite (Fap), phlogopite (Phl) and diopside (Di): fragments of the coarse-grained (**a**) and fine-grained (**b**) zones of the specimen. SEM (BSE) images of polished sections.

Sample 11 is orange–yellow sulfhydrylbystrite from the Malo-Bystrinskoe gem lazurite deposit. The mineral forms anhedral grains up to 0.2 mm across and partial pseudomorphs after lazurite in a metasomatic rock mainly composed of calcite, diopside, nepheline, lazurite, phlogopite, Sr-bearing plagioclase and Ca- and Ba-bearing stronalsite $Na_2(Sr,Ca,Ba)(Si_4Al_4O_{16})\cdot nH_2O$ (Figures 3 and 4). Plagioclase and stronalsite occur in the rock in minor amounts. For the chemical analyses of Sample 11, see Table 2. The empirical formula of Sample 11 based on $(Si,Al,Fe)_{12}(S_5^{2-})$ is $Na_{4.37}K_{2.22}Ca_{1.17}(Si_{6.12}Al_{5.87}Fe_{0.01}O_{24})(S_5)^{2-}(HS^-)_{0.76}S^{2-}_{0.10}Cl_{0.09}\cdot nH_2O$ (Z = 2, n << 1; the excess of sulfur over 5 atoms per formula unit is divided among HS^- and S^{2-}, taking into account the charge-balance requirement). The presence of a minor amount of H_2O molecules in Sample 11 was established using IR spectroscopy (see below).

Sample 12 is sulfhydrylbystrite from the Malo-Bystrinskoe deposit with the composition (wt.%): Na_2O 14.72, K_2O 6.89, CaO 4.85, Al_2O_3 27.44, SiO_2 31.49, S 15.60, Cl 0.15, –O=Cl −0.03, total 101.11, where S is the total sulfur belonging to S_5^{2-}, HS^- and S_4, in accordance with the Raman spectrum (see below). The oxygen equivalent for sulfur could not be calculated because the proportion of the sulfide groups is unknown. The empirical formula is $H_x(Na_{5.34}K_{1.65}Ca_{0.96})(Si_{5.89}Al_{6.04}Fe_{0.07}O_{24})(S^{total})_{5.47}Cl_{0.06}$ (Z = 2). The mineral forms

red–orange anhedral grains up to 0.4 mm across in a metasomatic rock mainly composed of calcite, diopside, nepheline, lazurite, afghanite, phlogopite, plagioclase and Ca- and Ba-bearing stronalsite $Na_2(Sr,Ca,Ba)(Si_4Al_4O_{16})\cdot nH_2O$.

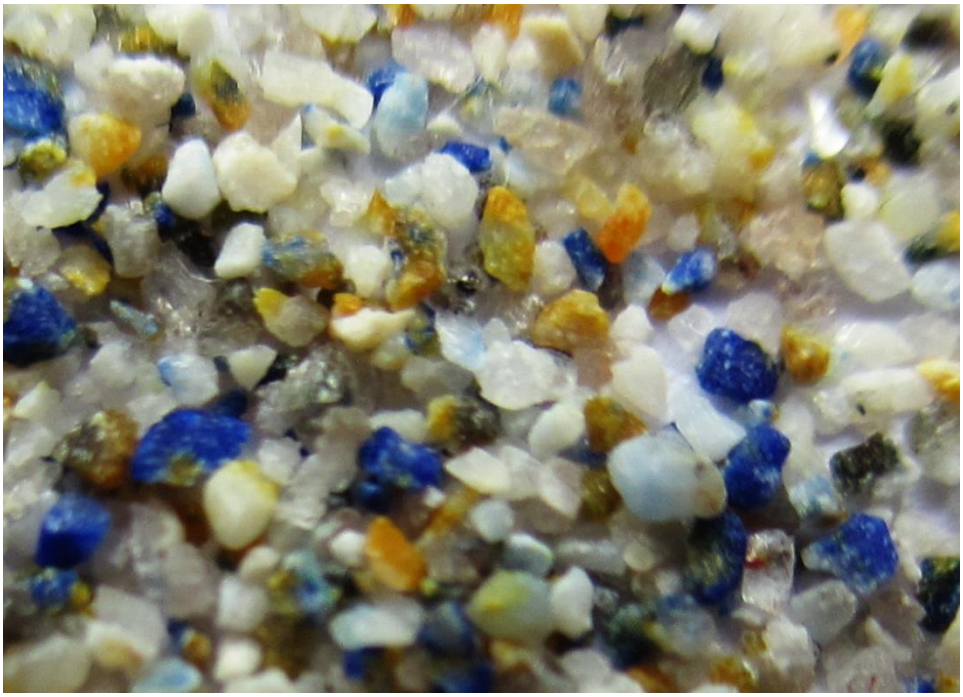

Figure 3. Crushed rock composed of orange–yellow sulfhydrylbystrite (Sample 11) intergrown with red–orange sulfhydrylbystrite variety (Sample 12), lazurite (deep blue), afghanite (pale blue), calcite (white), nepheline (brownish) and Sr-bearing feldspar (grey). FOV width: 12 mm.

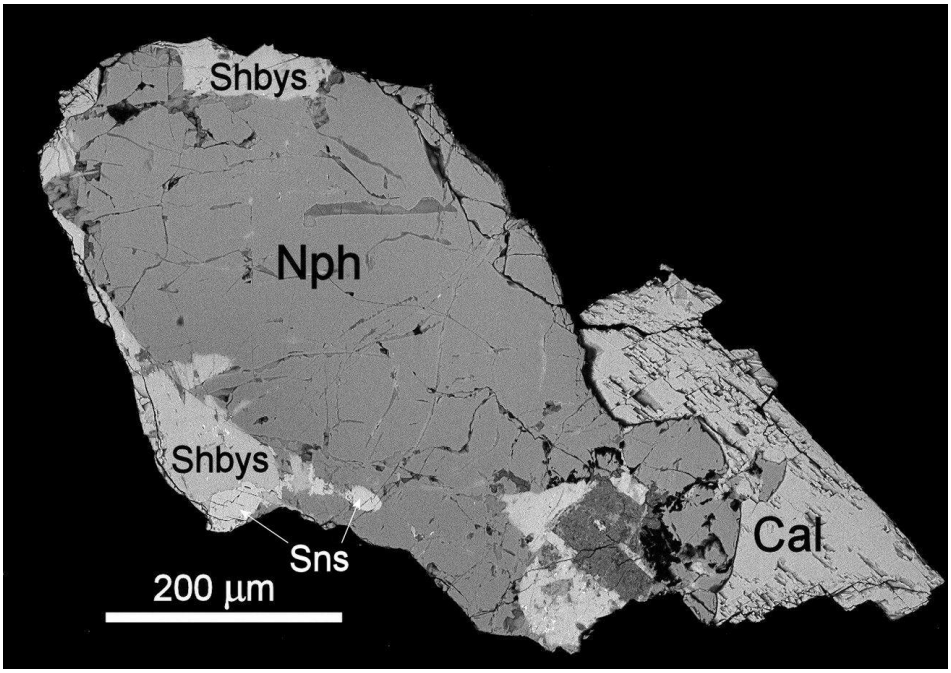

Figure 4. Mineral association of sulfhydrylbystrite (Shbys, Sample 11) with calcite (Cal), nepheline (Nph) and stronalsite (Sns). SEM (BSE) image of a polished section.

Table 2. Chemical composition (wt.%) of bystrite (Sample 9) and sulfhydrylbystrite (Sample 11).

Component	Sulfhydrylbystrite (for 19 Spot Analyses)			Bystrite (for 5 Spot Analyses)		
	Mean	Ranges	Standard Deviation	Mean	Ranges	Standard Deviation
Na_2O	11.89	10.59–13.14	0.63	18.70	18.38–19.31	0.28
K_2O	9.20	8.00–10.54	0.76	0.16	0.08–0.29	0.08
CaO	5.79	5.23–7.38	0.49	5.55	4.91–5.95	0.41
Al_2O_3	26.29	25.17–27.27	0.59	26.95	26.20–27.43	0.46
Fe_2O_3	0.07	0–0.35	0.11	0.03	0–0.11	0.05
SiO_2	32.35	31.52–34.72	0.74	32.68	31.88–33.64	0.73
S_5^{2-} HS^- S^{2-} S^0	14.08 2.21 0.28 -	15.68–17.34 (for total sulfur)	0.43 (for total sulfur)	14.87 0.51 - -	14.69–15.50 (for total sulfur)	0.31 (for total sulfur)
Cl^-	0.27	0–0.65	0.19	2.70	2.39–2.90	0.19
$-O\equiv S_5^{2-}$	−1.41	-	-	−1.48	-	-
$-O\equiv HS^-$	−0.53	-	-	−0.12	-	-
$-O\equiv S^{2-}$	−0.14	-	-	-	-	-
$-O\equiv Cl^-$	−0.06	-	-	−0.61	-	-
Total	100.29	-	-	99.94	-	-

Samples 13a and 13b are two varieties of the SO_3^{2-}-bearing analogue of marinellite-forming pale violet and deep violet grains, respectively, up to 1 mm across in a subvolcanic rock mainly composed of sanidine with subordinate biotite and minor nepheline and leucite (Figure 5). The specimens originate from Magliano, Rome, Latium, Italy. The chemical composition of Sample 13b based on six spot analyses is (wt.%, all sulfur was calculated as SO_3): Na_2O 14.01, K_2O 8.44, CaO 5.52, Al_2O_3 27.90, SiO_2 32.79, SO_3 9.72, Cl 1.09, H_2O (determined by the Alimarin method) 0.95, –O=Cl –0.26, total 100.18, which corresponds to the empirical formula $(Na_{29.78}K_{11.81}Ca_{6.49})(Si_{35.05}Al_{36.05}O_{24})(SO_4,SO_3)_{8.00}Cl_{2.03}(OH)_{0.49}\cdot 3.25H_2O$ (Z = 1). The crystal structure of Sample 13b was refined to an R-factor of 5.71% for 6819 independent reflections with $I > 2\sigma(I)$ [66]. The mineral is trigonal, in space group $P31c$ and the unit cell parameters are: a = 12.8727(2), c = 31.7393(5) Å and V = 4554.75(15) Å^3. The crystal chemical formula is $Na_{29.78}K_{11.82}Ca_{6.40}(Si_{36}Al_{36}O_{144})(SO_4)_6(SO_3)_2Cl_2(OH)_{0.40}\cdot 3.98H_2O$. The SO_3^{2-} groups dominate at an extra-framework site hosted by the liottite cage.

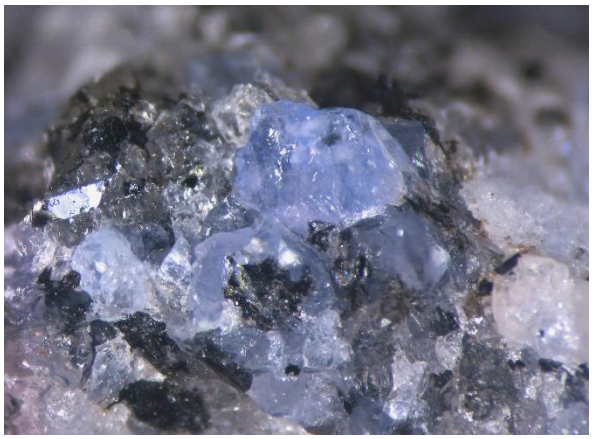

(**a**)

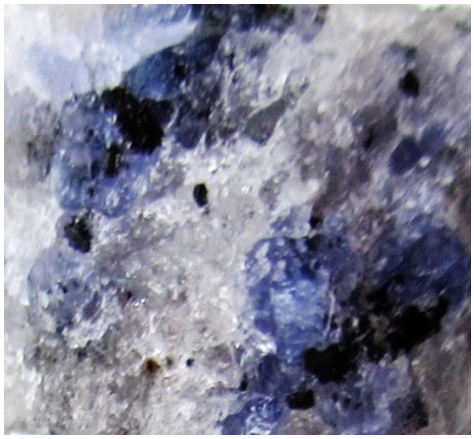

(**b**)

Figure 5. Grains of the SO_3^{2-}-bearing analogue of marinellite in association with sanidine (white) and biotite (black): Samples 13a (**a**) and 13b (**b**). Field of view widths: 3 mm (**a**) and 5 mm (**b**).

Sample 14 is the holotype specimen of the 30-layer cancrinite-group mineral biachellaite [67]. It occurs as colorless short-prismatic and tabular blocky crystals up to 1 cm (Figure 6) in a volcanic syenitic ejectum from the Biachella Valley, Sacrofano paleovolcano, Latium, Italy. The associated minerals are sanidine, diopside, andradite, leucite, haüyne, sacrofanite, steudelite, liottite and alloriite. The empirical formula of Sample 14 is $(Na_{3.76}Ca_{2.50}K_{1.44})(Si_{6.06}Al_{5.94}O_{24})(SO_4)_{1.84}Cl_{0.15}(OH)_{0.43}\cdot 0.81H_2O$ (Z = 15). The mineral is trigonal, in space group $P3$ and the unit cell parameters are a = 12.913(1), c = 79.605(5) Å and V = 11495(1) Å^3.

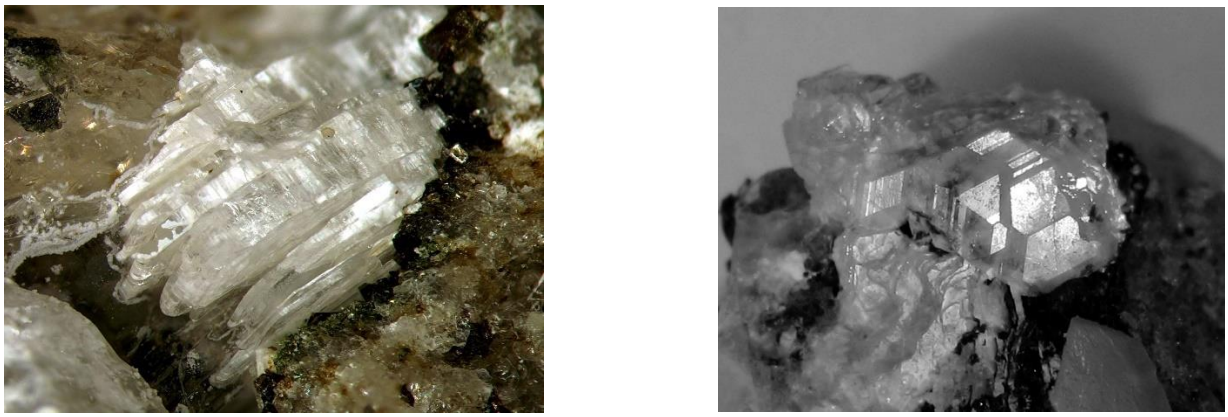

(**a**) (**b**)

Figure 6. Crystals of biachellaite. Field of view widths: 5 mm (**a**) and 6 mm (**b**).

Sample 15 is white S-bearing meionite from the Slyudyanka phlogopite deposit, Uluntuy gorge, Slyudyanka district. It is a fragment of a tetragonal prismatic crystal (4 cm long and 3 cm thick) from magnesian skarn mainly consisting of diopside and calcite. Its empirical formula is (Table 3, CO_3^{2-} calculated based on the charge balance requirement): $(Ca_{2.95}Na_{0.93}K_{0.13})(Si_{6.84}Al_{5.16}O_{24})(CO_3)_{0.605}(SO_4)_{0.23}Cl_{0.13}$.

Sample 16 is violet–blue meionite ("glaucolite") from the Slyudyanka river valley, Slyudyanka district. It is a fragment of old (beginning of 20th century) specimen deposited in the Fersman Mineralogical Museum of the Russian Academy of Sciences (Moscow) with catalogue number 54,413. Meionite forms coarse-grained nest (8 cm across), rimmed by light golden-brown phlogopite, in calcite marble. Its empirical formula is (Table 3, CO_3^{2-} calculated based on the charge balance requirement): $(Ca_{2.36}Na_{1.51}K_{0.05})(Si_{7.19}Al_{4.81}O_{24})(CO_3)_{0.645}(SO_4)_{0.01}Cl_{0.16}$.

Table 3. Chemical composition (wt.%) of scapolites.

Constituent	Sample 15	Sample 16
	Content (wt.%)	
Na_2O	3.05	5.21
K_2O	0.64	0.31
CaO	17.57	14.75
Al_2O_3	27.91	27.32
SiO_2	43.61	48.19
SO_3	1.97	0.10
Cl	0.58	0.68
–O=Cl	–0.13	–0.15
Total	95.20	96.41
Formula coefficients based on Si + Al = 12 *apfu*		

Na	0.93	1.51
K	0.13	0.05
Ca	2.95	2.36
Al	5.16	4.81
Si	6.84	7.19
S	0.23	0.01
Cl	0.15	0.16

2.2. Synthesis and Thermal Conversions

All syntheses of sodalite- and cancrinite-type compounds were performed under mild hydrothermal conditions at temperatures of 180 °C to 230 °C within 16–24 h. In order to obtain the framework aluminosilicates with incorporated S-bearing anions, we utilized the traditional process of geopolymers production, that involves an aluminosilicate precursor and a soluble alkaline medium, preferably Na or K hydroxide solutions. This method also simulates the crystallization conditions of sodalite- and cancrinite-group minerals in postmagmatic alkaline rocks. S-bearing sodalite-type phases were synthesized using a highly dispersed powder of metakaoline as an aluminosilicate source. The purity of metakaolinite was verified by the powder X-ray diffraction. The chemical composition of starting kaolin used in the experiments is as follows (wt.%): SiO_2 46.5, Al_2O_3 39.0, FeO 0.5 % and H_2O 14.0%.

Three salts with different sulfur oxidation degrees were used in the experiments: $Na_2S{\cdot}10H_2O$, $Na_2SO_3{\cdot}5H_2O$ and $Na_2S_2O_3$. The mixtures of the metakaoline powder (3 g), S-bearing salts (3 g) and 8M NaOH (5 mL) aqueous solution were loaded to the hydrothermal reactor with a 25 mL polypropylene (PP) bottle, stirred for 10 min and placed into the muffle furnace. In the experiment with $Na_2S_2O_3$, 1.5 g of $CaCl_2$ was added to the charge. After the completion of the experiments, the samples were washed with distilled water and dried in a cabinet dryer oven.

The thermal transformations of S-bearing extra-framework anions in the synthesized materials under different redox conditions were studied by the heating of initial powders in a muffle furnace at 700–800 °C for 6 h in uncoated crucibles in contact with atmospheric air (oxidizing conditions) and crucibles with carbon tablets (reducing conditions). The thermal treatment conditions and crystallographic data of the treatment products are given in Table 4. The cell parameters and especially the space group assignments were determined from powder X-ray diffraction patterns, taking into account the systematic absences of the reflections. All the compounds of the products belong to the sodalite and/or cancrinite structure types. The chemical data for the synthetic phases are presented in Table 5. For the product of Experiment 1b, containing both SO_4^{2-} and polysulfide groups (mainly, $S_3^{\bullet-}$ and S_4) in unknown proportions (see below), the oxygen equivalent of polysulfide groups could not be calculated. All the sulfur in this sample is given as SO_3, which resulted in a high analytical total.

The thermal conversions of Sample 5 were carried out in two stages. In the first stage, the method of the double quartz tube was applied. The samples were heated for three days at 700 °C in a reducing atmosphere (over the Fe-FeS buffer). As a result, a SO_4^{2-}-free and (HS^-,S^{2-},$S_2^{\bullet-}$,$S_4^{\bullet-}$)-bearing sodalite-type material (so-called "S-sodalite") was obtained [13]. On the next step, this material was annealed in air, in a muffle furnace at 600 °C and 700 °C, from 1 to 256 h together with CaF_2 (cubic, with a = 5.4634 Å) that was used as an internal standard for the determination of the unit cell parameter of the sample under investigation. The annealing in the air resulted in gradual transformations of the above-listed sulfide groups into SO_4^{2-} and $S_3^{\bullet-}$ [13].

Table 4. Data on the experimental conditions and crystallographic characteristics of the products.

Experiment	S-Bearing Salt	Treatment Conditions	Color of the Product	Space Group, Unit Cell Parameters
1	$Na_2S \cdot 10H_2O$	Initial product of synthesis	Pale blue	*P*4-3*n*, *a* = 8.9217(3) Å, *V* = 710.14(1) Å^3
1a	$Na_2S \cdot 10H_2O$	*t* = 800 °C, 6 h, muffle furnace	White	*P*23, *a* = 9.0878(1) Å, *V* = 750.55(1) Å^3
1b	$Na_2S \cdot 10H_2O$	*t* = 700 °C, 6 h, muffle furnace with carbon tablets	Blue	*P*23, *a* = 9.0926(1) Å, *V* = 751.74(1) Å^3
2	$Na_2SO_3 \cdot 5H_2O$	Initial product of synthesis	White	$P6_3$, *a* = 12.7004(7) Å, *c* = 5.1768(7) Å, *V* = 723.2(1) Å^3 and *P*4-3*n*, *a* = 8.8867(3) Å, *V* = 701.8(1) Å^3
2a	$Na_2SO_3 \cdot 5H_2O$	*t* = 800 °C, 6 h, muffle furnace	White	*P*23, *a* = 9.0928(1) Å, *V* = 751.79(1) Å^3
2b	$Na_2SO_3 \cdot 5H_2O$	*t* = 700 °C, 6 h, muffle furnace with carbon tablets	White with pale blue hue	*P*23, *a* = 9.0913(1) Å, *V* = 751.41(1) Å^3
3	$Na_2S_2O_3$	Initial product of synthesis	Light green	*P*3, *a* = 12.6780(3) Å, *c* = 5.1905(2) Å, *V* = 722.5(1) Å^3

Table 5. Representative chemical data (wt.%) of the products of synthesis and analyses. The analyses numbers correspond to Experiment 1 (1), Experiment 1a (2), Experiment 1b (3), Experiment 2 (4), Experiment 2a (5), Experiment 2b (6) and Experiment 3 (7).

Analysis No. → Component ↓	1	2	3	4	5	6	7
	Content (wt.%)						
Na_2O	24.3	15.36	19.23	19.14	21.43	22.68	16.00
K_2O	-	0.67	5.15	-	-	1.54	-
CaO	-	-	-	-	-	0.18	4.69
Al_2O_3	33.32	33.60	37.51	32.98	30.79	32.71	30.62
Fe_2O_3	-	-	-	-	0.33	0.53	0.33
SiO_2	38.46	37.94	42.22	38.52	38.19	41.46	40.66
HS^-	5.39	-	-	-	-	-	-
SO_3	-	12.79	14.29	-	8.10	3.66	-
SO_2	-	-	-	6.35	-	-	-
S_2O_3	-	-	-	-	-	-	9.56
Total	100.24 *	100.36	118.40	94.99	98.85	102.75	100.57 *
	Formula coefficients calculated on 12 Si + Al + Fe atoms per formula unit						
Na	7.27	4.61	5.18	6.15	6.67	6.56	4.83
K	-	0.13	0.91	-	-	0.29	-
Ca	-	-	-	-	-	0.03	0.78
Al	6.06	6.13	6.14	5.90	5.83	5.75	5.62
Fe	-	-	-	-	0.04	0.06	0.04

Si	5.94	5.87	5.86	6.10	6.13	6.19	6.34
S^{total}	1.51	1.49	1.49	0.91	0.98	0.41	1.60

* Oxygen equivalents of S-bearing groups are subtracted.

2.3. Analytical Methods

The diffuse absorption spectra in the near infrared, visible and ultraviolet (NIR/Vis/UV) ranges were measured at room temperature using a Lambda 950 spectrophotometer (Perkin-Elmer, Shelton, CT, USA) [12,13]. In particular, the absorption spectra of the platelets of Sample 1 (about 1 mm thick) were measured in the transmission mode through a circular diaphragm 0.8 mm in diameter. The spectra were measured in an integrating sphere at room temperature. To do this, small crystals of the studied mineral were placed in a quartz test tube, transparent in the region of 250–2000 nm, and the test tube was placed in an integrating sphere.

The ESR spectra were measured with a RE-1306 X-band spectrometer (KBST, Smolensk, Russia) with a frequency of 9.3841 GHz at room temperature and 9.1841 GHz at 77 K [12,13]. For low-temperature measurements, a quartz ampoule with the sample was placed in a flooded cryostat.

In order to obtain the IR absorption spectra, the powdered samples were mixed with anhydrous KBr, pelletized and analyzed using an ALPHA FTIR spectrometer (Bruker Optics, Karlsruhe, Germany) at a resolution of 4 cm^{-1} as described in [5,6,8,12,13]. Sixteen scans were collected for each spectrum. The IR spectrum of an analogous pellet of pure KBr was used as a reference.

The Raman spectra of the natural samples have been obtained for randomly oriented grains using an EnSpectr R532 spectrometer based on an OLYMPUS CX 41 microscope (Enhanced Spectrometry, San Jose, CA, USA) coupled with a diode laser (λ = 532 nm) at room temperature [5,8,12,13]. The spectra were recorded in the range from 100 to 4000 cm^{-1} with a diffraction grating (1800 gr mm^{-1}) and spectral resolution of about 6 cm^{-1}. The output power of the laser beam was in the range from 5 to 13 mW. The diameter of the focal spot on the sample was 5–10 μm. The backscattered Raman signal was collected with a 40× objective; the signal acquisition time for a single scan of the spectral range was 1 s and the signal was averaged over 50 scans. Crystalline silicon was used as a standard.

The Raman spectra of the synthesized samples were acquired with a confocal Raman microscope JY Horiba XPloRA at the Department of Petrology and Volcanology (Geological Faculty, Lomonosov Moscow State University, Moscow, Russia). A laser beam with a 532 nm wavelength and 12 mW power was used as an excitation source. The spectra were collected in the range 100–3900 cm^{-1} with a 1800 gr/mm diffraction grating, a 10× objective and 40 s accumulation time per each window.

The powder X-ray diffraction investigation of the annealed Sample 5 was carried out with a DRON-3 diffractometer (Burevestnik, St. Petersburg, Russia) using Fe-Kα (with a Mn filter) and Cu-Kα (with a Ni filter) radiations [6]. The sub-cell *a* parameter was determined using the (440) reflection with an accuracy within ±0.001 Å.

The single-crystal XRD studies were carried out using an Xcalibur S diffractometer (OXFORD DIFFRACTION, Oxford, GB) equipped with a CCD detector (Mo*K*α radiation).

The powder XRD data for the synthesized powders of S-bearing feldspathoids were collected using a Bruker D8 Discover diffractometer in the Bragg-Brentano geometry, 2Θ range of 5–120° and 2Θ step of 0.02° using CuKα radiation (λ = 1.54018 Å), at an accelerating voltage of 40 kV, current of 40 mA and time per step of 1.5 s.

The chemical composition of sample 15 was analyzed by means of a Hitachi FlexSEM 1000 equipped with an Xplore Contact 30 EDS-detector and Oxford AZtecLive STD system of analysis (15 kV, 5 nA, 2 μm) [6]. The standards and analytical lines are: NaKα–albite, AlKα–kyanite, SiKα–SiO_2, SKα–$BaSO_4$, ClKα–TlCl, KKα–KBr and

CaKα–wollastonite. The contents of other elements with an atomic number higher than that of Be are below the detection limits.

The EDS-mode electron microprobe analyses of the other samples were carried out on an analytical suite, including a digital scanning electron microscope Tescan VEGA-II XMU equipped with an energy-dispersive spectrometer (EDS) INCA Energy 450 with a semiconducting Si (Li) detector Link INCA Energy and wave-dispersive spectrometer (WDS) Oxford INCA Wave 700, produced by Tescan Orsay Hld., Brno, the Czech Republic. The analyses were performed at an accelerating voltage of 20 kV, a current of 120 to 150 pA and a beam diameter of 120 nm. The diameter of the excitation zone was below 5 μm. The following standards were used: CaF_2 for F, albite for Na, synthetic Al_2O_3 for Al, wollastonite for Ca, potassium feldspar for K, SiO_2 for Si, Fe metal for Fe and FeS_2 for S. The contents of the other elements with atomic numbers >6 are below the detection limits.

The proportion of sulfide and sulfate sulfur in the experiments with the thermal conversions of Sample 5 was determined in the Central Research Geological Exploration Institute of Nonferrous and Noble Metals (Moscow) by X-ray photoelectron spectroscopy (XPS) [6]. The spectra were acquired using a Riber LAS-3000 spectrometer with a hemispherical electron detector (Riber, Bezons, France), with a retention potential and non-monochromatic Al radiation (AlKα = 1486.6 eV) at an anode current of 20 mA and an accelerating voltage of 10 kV. The C 1 s peak at 285 eV was used to correct the binding energies for the charging of the surface. The obtained S 2p peaks are $2p_{3/2}$–$2p_{1/2}$ spin–orbit doublets. In order to obtain accurate binding energy values, the peaks were deconvoluted using a special program allowing for a nonlinear background and Voigt function used to approximate the peak shapes. The peaks were assigned to a particular sulfur species based on $2p_{3/2}$ doublet components using the available published data [68].

3. Results

3.1. Minerals of the Cancrinite-Cancrisilite-Vishnevite Solid-Solution Series

The aluminosilicate frameworks of minerals belonging to the cancrinite-cancrisilite-vishnevite solid-solution series have a hexagonal symmetry and a cancrinite-type topology with wide channels and columns of cancrinite cages running along the *c* axis. There is a wide isomorphism between cancrinite and vishnevite, whereas cancrisilite is usually S-depleted [64]. In this paper, we report data on an unusual S- and P-bearing cancrisilite variety (Sample 3, see Table 1). Its IR and Raman spectra are presented in Figures 7 and 8, respectively. The spectra of cancrinite (Sample 1) and CO_3-bearing vishnevite (Sample 2) are given in these figures for a comparison.

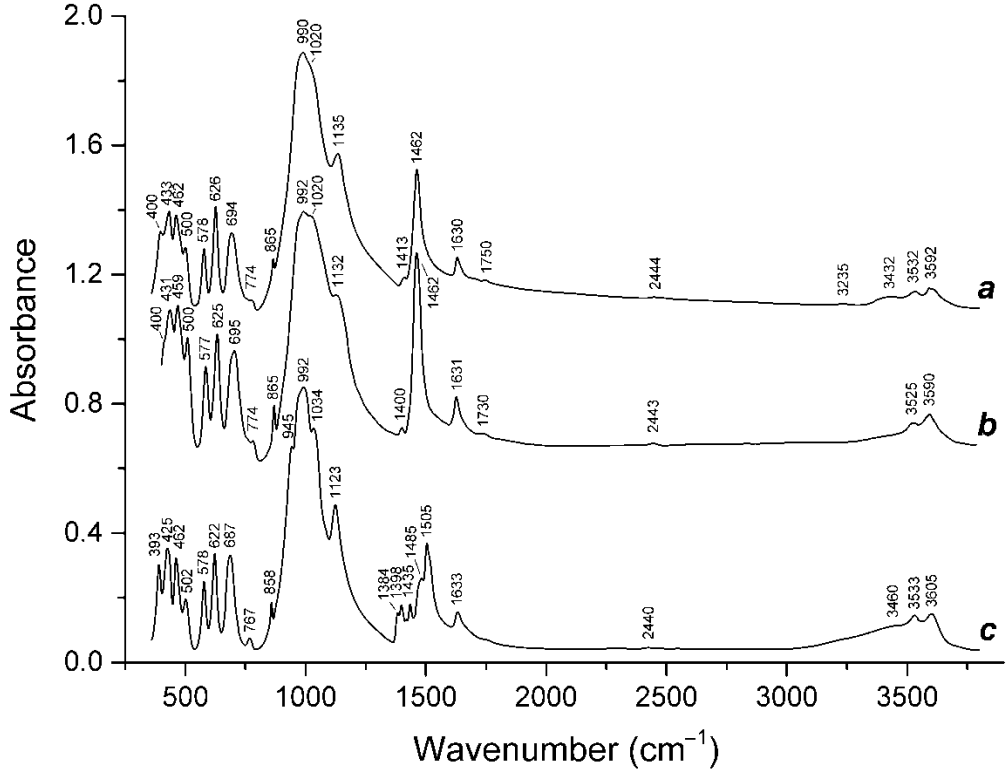

Figure 7. IR spectra of (**a**) S- and P-bearing cancrisilite (Sample 3), (**b**) typical cancrisilite (Sample 4) and (**c**) cancrinite (Sample 1).

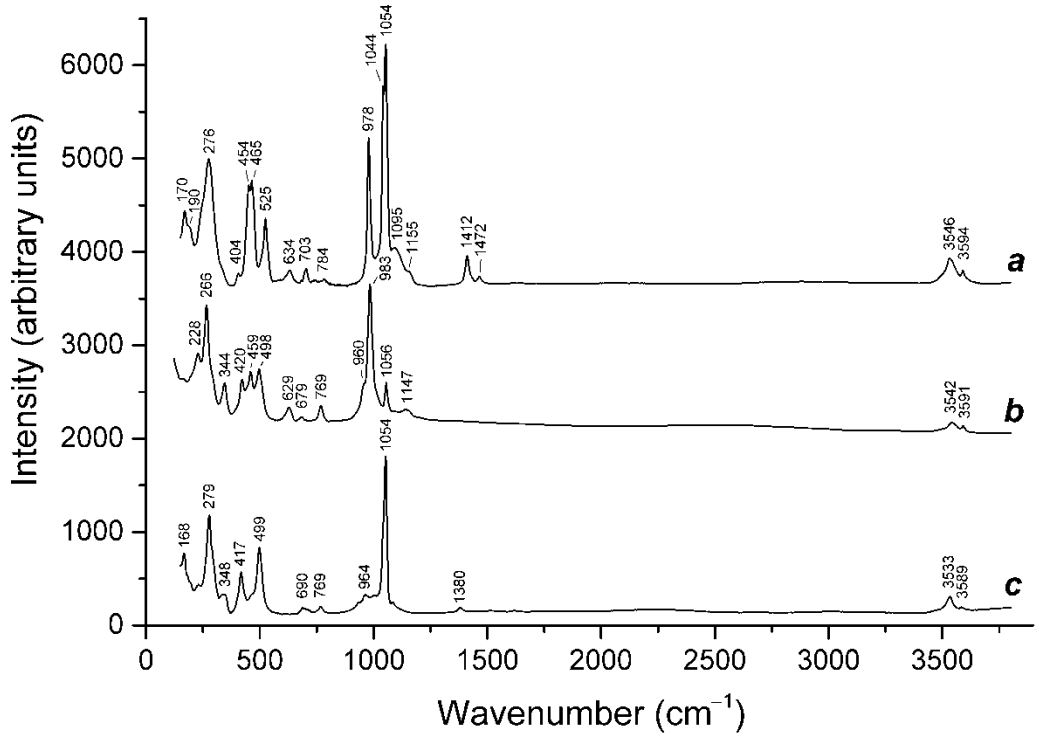

Figure 8. Raman spectra of (**a**) S- and P-bearing cancrisilite (Sample 3), (**b**) CO_3^{2-}-bearing vishnevite (Sample 2) and (**c**) cancrinite (Sample 1).

The IR spectra of S-rich and S-poor cancrisilites are similar. All bands in the range of 3200–3700 cm^{-1} correspond to H_2O molecules. The S-rich Sample 3 differs from the common cancrisilite Sample 4 by the presence of additional bands of H_2O molecules at

3235 and 3432 cm^{-1}, the enhanced intensity of the peak at 1135 cm^{-1} (overlapping bands of Si–O–Si stretching vibrations and asymmetric stretching vibrations of SO_4^{2-} anions), as well as lowered intensities of the bands of asymmetric stretching and out-of-plane bending vibrations of the CO_3^{2-} anions (at 1462 and 865 cm^{-1}, respectively). In the crystal structure of cancrisilite, CO_3^{2-} anions occupy three independent sites. The bands at 1462 and 1400–1413 cm^{-1} in the IR spectra of cancrisilite correspond to common vibrations of two identical CO_3^{2-} groups in which changes in the dipole moment are parallel and antiparallel, respectively [69]. The IR spectrum of cancrinite in this region (curve *c* in Figure 7) is more complex, which reflects the presence of numerous independent sites of CO_3^{2-} anions in the crystal structure of this mineral [70].

The Raman spectrum of S-rich cancrisilite (curve a in Figure 8) is more informative. It contains bands of bending vibrations of SO_4^{2-} at 454 and 465 cm^{-1} [the $E(\nu_2)$ mode] and 634 cm^{-1} [the $F_2(\nu_4)$ mode] as well as stretching modes of SO_4^{2-} at 978 cm^{-1} [symmetric vibrations, the $A_1(\nu_1)$ mode] and 1095 cm^{-1} with a shoulder at 1155 cm^{-1} [asymmetric vibrations, the $F_2(\nu_3)$ mode]. The nondegenerate $A_1(\nu_1)$ band is not split, which indicates that the SO_4^{2-} anions occupy a single site. The Raman bands of in-plane bending, symmetric stretching and asymmetric stretching vibrations of the CO_3^{2-} anionic groups are observed at 703, 1044 + 1054 and 1412 + 1472 cm^{-1}, respectively. The doublet 1044 + 1054 cm^{-1} corresponding to a nondegenerate mode may indicate that the CO_3^{2-} groups are locally nonequivalent and SO_4^{2-} substitutes the CO_3^{2-} groups only at one site. A comparison of the Raman spectra of Samples 1, 2 and 3 shows that the band at 1044 cm^{-1} in the Raman spectrum of Sample 3 may correspond to the CO_3^{2-} anions, whose local environment contains SO_4^{2-}.

The assignment of the band at 525 cm^{-1} in the Raman spectrum of S-rich cancrisilite is ambiguous. This band is absent in the Raman spectra of other minerals with the cancrinite-type framework. The strong band at 520 cm^{-1} in the Raman spectrum of hannebachite, $Ca(SO_3)\cdot 0.5H_2O$ was tentatively assigned to the $E(\nu_2)$ mode of SO_3^{2-} [71]. On the other hand, a strong Raman band at 523–530 cm^{-1} is a characteristic feature of the S_7 molecule, along with the bands at 237–239, 355–358, 400 and 481 cm^{-1} [48].

3.2. Isomorphism of Bystrite and Sulfhydrylbystrite

Bystrite was first described as a four-layer cancrinite-group mineral with the simplified formula $Ca(Na,K)_7(Si_6Al_6O_{24})(S_3)_{1.5}\cdot H_2O$ [72]. Subsequent investigations have shown that the samples were initially considered as Cl-bearing K-deficient and Cl-poor K-rich varieties of bystrite are different mineral species, bystrite and sulfhydrilbystrite, with the idealized formulae $Na_7Ca(Al_6Si_6O_{24})(S_5^{2-})Cl^-$ and $Na_5K_2Ca(Al_6Si_6O_{24})(S_5^{2-})(SH^-)$, respectively [73,74].

The IR spectra of these minerals published earlier are of a poor quality and contain bands of different impurities (mainly, calcite and adsorbed water). The IR spectra of bystrite and sulfhydrylbystrite obtained in this work (Figure 9) are similar. The distinctive features of sulfhydrylbystrite are the bands at 3565, 3460 and 1645 cm^{-1} corresponding to the stretching and bending vibrations of the H_2O molecules as well as the weak band at 2556 cm^{-1} corresponding to the stretching vibrations of the HS^- anion. Weak bands at 3430 and 1628 cm^{-1} in the IR spectrum of bystrite are related to the adsorbed water.

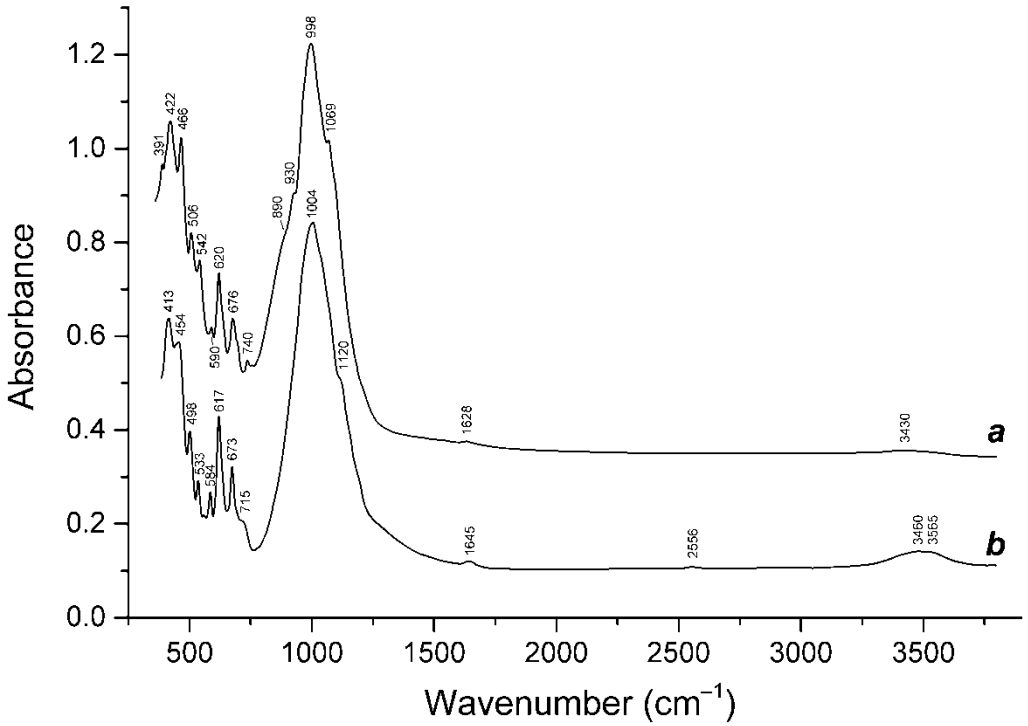

Figure 9. Infrared spectra of (**a**) bystrite (Sample 9) and (**b**) sulfhydrylbystrite (Sample 12).

According to the data of the X-ray structural analysis [73,74], bystrite and sulfhydrylbystrite contain the S_5^{2-} anion that is most thermodynamically favored among the S_n^{2-} anions, with the *n* ranging from 2 to 8 (the order of decreasing stability in the aqueous solution is S_5^{2-} >> S_6^{2-} > S_4^{2-} >> S_7^{2-} > S_3^{2-}>> S_8^{2-} > S_2^{2-} [63]). Neither the neutral cyclic S_5 molecule nor the radical anion $S_5^{\bullet-}$ have definitely been observed in the solution or in the solid state.

The wavenumbers of fundamental S–S stretching vibrations predicted for S_5^{2-} coordinated by Li^+ are 471, 463 and 416 cm^{-1} [63]. Similar bands are observed in the IR spectra of bystrite and sulfhydrylbystrite in the ranges of 413–422 and 454–466 cm^{-1}. No bands in these ranges are in the IR spectrum of carbobystrite, a carbonate cancrinite-group mineral with the bystrite-type framework [75].

Unlike IR spectroscopy, Raman spectroscopy is very sensitive to the presence of the HS^- anions. The wavenumbers of the Raman band of the H–S stretching vibrations of HS^- in sodalite-group minerals and products of their heating under reducing conditions are in the range of 2550–2580 cm^{-1} [7,13]. Thus, the band at 2562 cm^{-1} in the Raman spectrum of sulfhydrylbystrite (Figure 10) should be assigned to the HS^- anion occurring in the cancrinite cage, in accordance with the structural data [73].

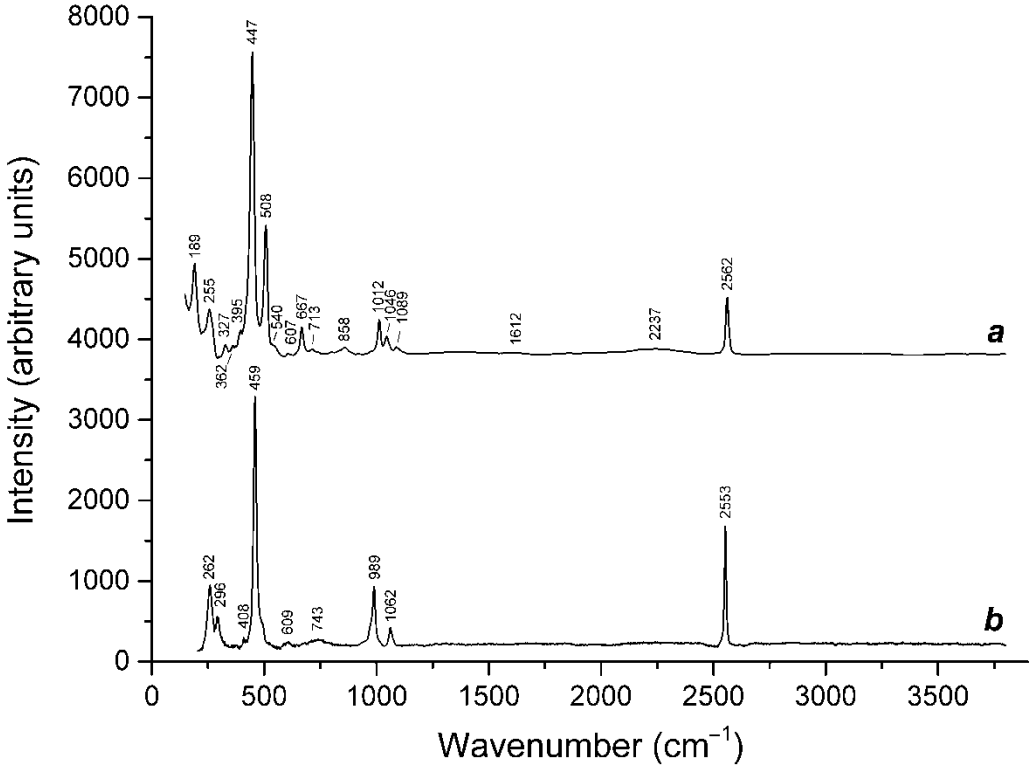

Figure 10. Raman spectra of (**a**) red–orange sulfhydrylbystrite (Sample 12) and (**b**) sapozhnikovite $Na_8(Al_6Si_6O_{24})(HS)_2$ from the Lovozero alkaline massif, Kola Peninsula, Russia. Baselines of both spectra are corrected.

The doublets 447 + 508 and 189 + 255 cm^{-1} in the Raman spectrum of sulfhydrylbystrite are close to the bands of bending modes of the aluminosilicate framework and lattice acoustic modes, respectively, but taking into account the high intensities of these peaks, they should be considered as S–S stretching and S–S–S bending bands of S_5^{2-}, respectively, maybe overlapping with the much weaker bands of the framework vibrations. The weak band at 2237 cm^{-1} in the Raman spectrum of sulfhydrylbystrite may correspond to trace amounts of hydrated proton complexes with strong hydrogen bonds and the O···O distances of 2.5–2.6 Å [76]. Such complexes could be formed as a result of the partial dissociation of HS^- and the subsequent solvatation of H^+ by the H_2O molecule which are present in the structure of the studied sample, according to the IR spectroscopy data. The weak band at 607 cm^{-1} is due to the stretching vibrations of the $S_2^{\bullet-}$ radical anion occurring in sulfhydrylbystrite in trace amounts. Similar bands (at 609 and 605 cm^{-1}) observed in the Raman spectra of sapozhnikovite (Figure 10) and bolotinaite (described as a F-rich sodalite-group mineral [8]) also correspond to $S_2^{\bullet-}$, that is the cause of the strong luminescence of all these minerals under a laser beam. An additional source of luminescence of feldspathoids is Fe^{3+} [77]. In particular, a broad Raman band of sapozhnikovite in the range of 800–4500 cm^{-1} is a superposition of luminescence from $S_2^{\bullet-}$ and Fe^{3+} (see Figure 11).

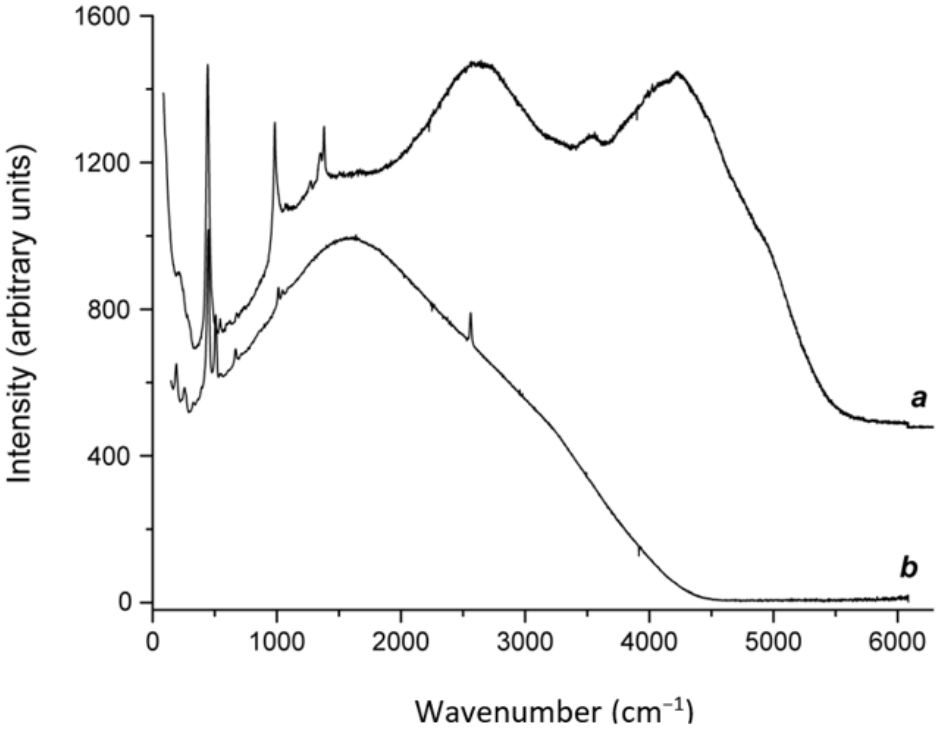

Figure 11. Uncorrected Raman spectra of (**a**) red–orange sulfhydrylbystrite (Sample 12) and (**b**) sapozhnikovite.

The wavenumbers of the strongest Raman bands of *cis*-S_4 (a red chromophore) calculated at the B3LYP/6-31G(2df) level are equal to 330, 373 and 674 cm^{-1} [48]. Similar bands (at 327–328, 362–363, 394–396 and 667–668 cm^{-1}) are present in the Raman spectrum of red–orange sulfhydrylbystrite (Sample 12, Figure 10) and orange–yellow bystrite (Sample 10, Figure 12). However, these bands are not observed in the Raman spectrum of yellow bystrite (Sample 9, Figure 12).

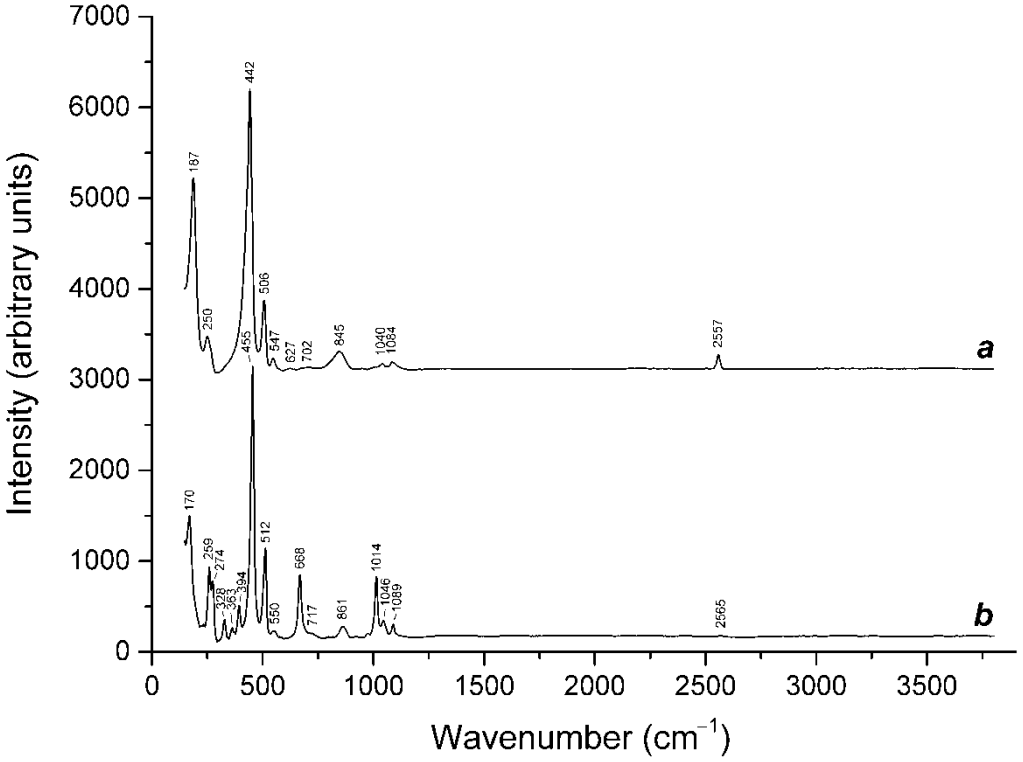

Figure 12. Raman spectra of (**a**) yellow bystrite (Sample 9) and (**b**) orange–yellow bystrite (Sample 10).

The bands in the range of 845–858 cm^{-1} correspond to the first overtone of the bands in the range of 442–455 cm^{-1}. All other bands in the Raman spectrum of sulfhydrylbystrite correspond to the stretching and bending vibrations of the framework. The very weak bands at 975 and 2565 cm^{-1} in the Raman spectrum of orange–yellow bystrite (Sample 10) indicate the presence of trace amounts of the SO_4^{2-} and HS^- anions, respectively.

3.3. Thermal Transformations of S$_4$-Bearing Haüyne and S-Sodalite–Haüyne Miscibility

The Raman spectra of S$_4$-bearing haüyne (Sample 5) and products of its thermal conversions are given in Figure 13. Photos of the heating products are presented in Figure 14. All the Raman bands of the initial Sample 5 in the range of 400–2600 cm^{-1}, except the band of SO_4^2 at 983 cm^{-1}, correspond to $S_3^{\bullet-}$. The Raman spectrum is very sensitive to the $S_3^{\bullet-}$ radical anion that is a strong blue chromophore. Therefore, despite a low content of $S_3^{\bullet-}$ in Sample 5, the bands of this species in its Raman spectrum are most strong. The wavenumbers (cm^{-1}) and assignment of the Raman bands of Sample 5 preheated at 700 °C under reducing conditions are as follows: 453–stretching vibrations of the $[(HS)^-Na_4]^{3+}$ cluster; 547–$S_3^{\bullet-}$ symmetric stretching (ν_1) mode; 596–stretching vibrations of the $[(S^{2-})Na_4]^{2+}$ cluster and/or $S_2^{\bullet-}$ stretching mode; 728–O–C–O bending vibrations of oxalate anions; 850–C–C stretching vibrations of oxalate anions; 989–framework stretching vibrations; 1064–CO_3^{2-} symmetric stretching vibrations; 1350–symmetric C–O stretching vibrations of oxalate anions, 1605–antisymmetric C–O stretching vibrations of oxalate anions; 1909–overtone or a combination mode; and 2556–HS^- stretching mode. All the observed Raman bands Sample 5 heated at 800 °C in the air (Figure 13) correspond to $S_3^{\bullet-}$ because the intensities of the Raman bands of other components are below noise level.

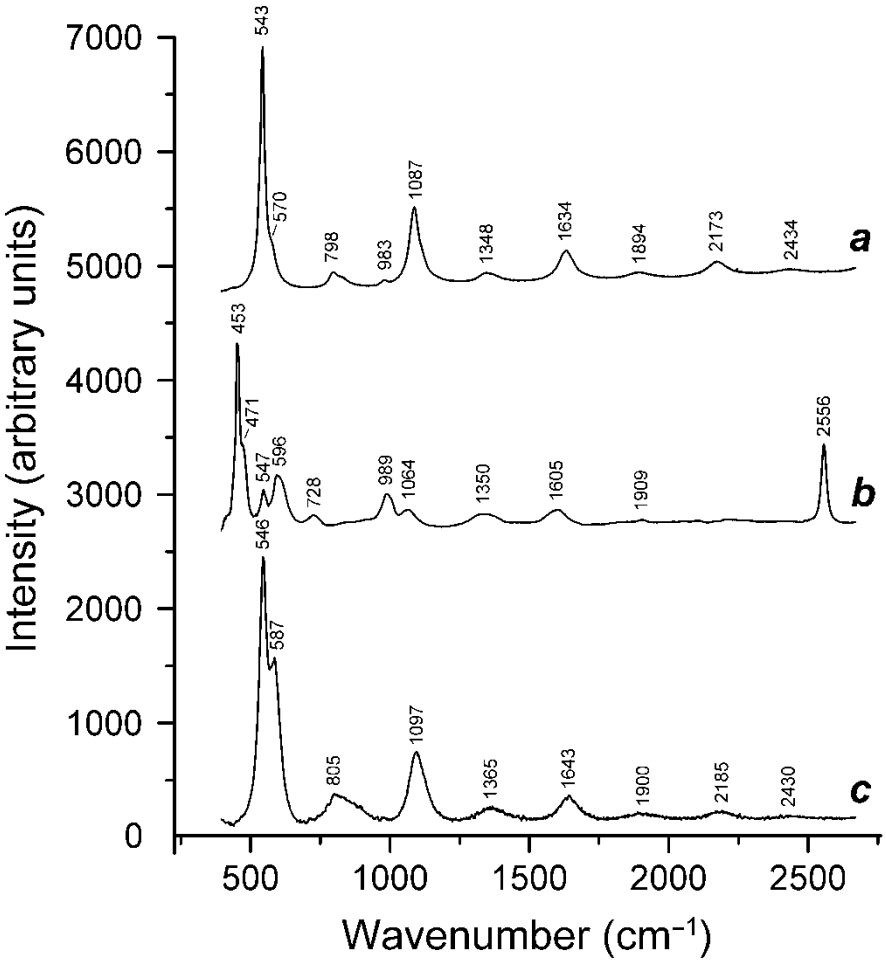

Figure 13. Raman spectra of (**a**) initial S_4-bearing haüyne (Sample 5), (**b**) Sample 5 preheated for three days at 700 °C, over the Fe-FeS buffer and (**c**) preheated Sample 5 additionally annealed at 800 °C in air for one day.

Based on Raman, the ESR and IR spectroscopy data, Sample 5 which preheated at 700 °C over the Fe-FeS buffer for three days, is sulfate-free and contains HS^- and S^{2-} anions as well as subordinate amounts of $S_2^{\bullet-}$ and $S_4^{\bullet-}$ radical anions [13]. The presence of $S_2^{\bullet-}$ is the cause of the yellow–brown color of the preheated sample. A subsequent annealing in the air results in a change in the color, first to green (Figure 14) and then to blue because of the restoration of the $S_3^{\bullet-}$ radical anion (a blue chromophore) [13].

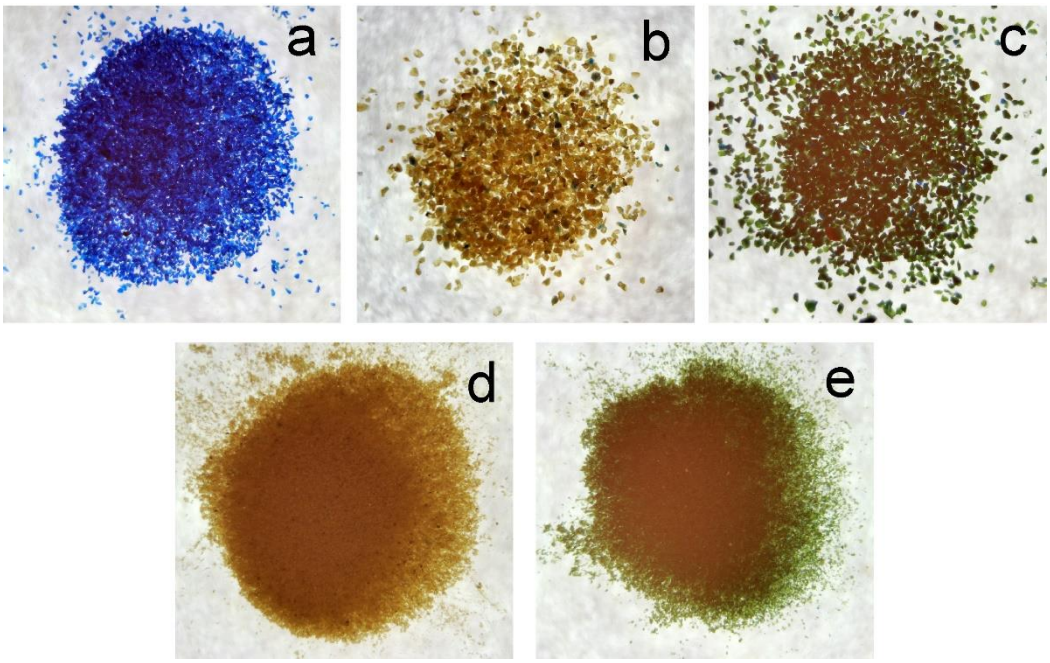

Figure 14. Color changes during heating of Sample 5: (**a**) initial sample, (**b**) 0.1–0.2 mm fraction preheated at 700 °C during 3 days, over the Fe-FeS buffer, (**c**) preheated 0.1–0.2 mm fraction after annealing at 800 °C during 24 h in air, (**d**) <0.04 mm fraction preheated at 700 °C during 3 days, over the Fe-FeS buffer and (**e**) preheated <0.04 mm fraction after annealing at 800 °C during 24 h in air.

The XPS spectrum of Sample 5 annealed with a buffer is a section of the general signal increase in the range of the binding energies between those of S^{2-} and SO_3^{2-} (160–167 eV), without a clear separation of the individual peaks. However, the XAS method, which is more sensitive to the composition of the sample volume than XPS, revealed the features of the XANES S K-edge spectrum, which were initially interpreted as S^{2-} in two nonequivalent structural positions [78]. However, Raman spectroscopy shows the presence of large amounts of HS^- anions in this sample [13]. After annealing in air at 800 °C for 1 day, the XPS spectrum detects only oxidized forms of sulfur, SO_4^{2-} and SO_3^{2-}.

The results indicate that the Ca-bearing S-sodalite obtained from natural $S_3^{\bullet-}$-bearing haüyne can be transformed into phases containing extra-framework radical anions, the composition of which is determined by the redox conditions, partial pressures of the volatile components (fS_2 and fSO_2) and the conditions of the subsequent thermal treatment.

The transformation of the sulfide form into the sulfate form was studied in air at 600 and 700 °C by varying the heating time of the sample. The composition of the formed phases was determined based on the value of the unit cell parameter. The unit cell parameters of the sulfate and sulfide end-members of the MX_2 isomorphic series, where M = $[(Na,Ca)_8(Si,Al)_{12}O_{24}]^{4-}$, X = SO_4^{2-}, S^{2-}, were estimated as follows. For the sulfate end member, the value of 9.085 Å is accepted according to the data of the study of cubic $S_3^{\bullet-}$-bearing haüyne with the highest SO_4^{2-}/S ratios (where S is the total amount of sulfide sulfur) and the data of the long-time experiments on the annealing of lazurite in the range of 600–800 °C. The reproducibility of this value is no worse than ±0.003 Å. The situation with the sulfide end member is less clear. The value of the unit cell parameter for it varies from 8.876 to 8.944 Å [79–81].

The causes of the variations are the variable amount of the haüyne component of the solid solution and partial oxidation of sulfur by atmospheric air. In further calculations, we used the parameter a = 8.910 Å, the average between the two extreme values indicated above. Under the assumption that Vegard's law is in force for this system, the dependence of the unit cell parameter on the fraction of the sulfate end member [MSO_4] can be described by the following formula:

$$a\ (Å) = 8.91 + 0.00175 \cdot [MSO_4]\ (mol.\%) \quad (1)$$

The data on the kinetics of the thermal transformations during the annealing (at 600 °C and 700 °C, in air) of Sample 5 preheated over the Fe-FeS buffer are presented in Table 6. The initial sulfide sample had *a* parameter of 8.944 Å, which may be due to the presence of minor amounts of $S_4^{\bullet-}$ [13].

Table 6. Experimental data on thermal transformations during annealing of Sample 5 preheated over the Fe-FeS buffer.

Annealing Time, h	Parameters of Cubic Subcells, Å *	Content of the MSO_4 Component, Mol.% **	
		Sulfide Phase	Sulfate-Rich Phase
T = 600 °C			
1	8.945	-	20
2	8.949	-	22
4	8.950	-	23
8	8.953	-	25
16	8.961	-	29
32	8.969	-	34
64	8.980, 9.069	91	40
128	8.988, 9.080	97	45
256	8.992, 9.078	96	47
T = 700 °C			
1	8.975, 9.032	70	37
2	8.982, 9.042	75	41
4	8.984, 9.059	85	42
8	9.076	95	-
16	9.083	99	-

* Two parameters are given for two-phase products. ** According to Equation (1).

The theoretical analysis of the miscibility of the components in this system was carried out in the framework of the Urusov theory [82–84] in the approximation of asymmetric regular solutions and in modification for complex aluminosilicate groups [84]. The value of the mixing energy is determined as $Q = 4338$ cal/mole, which gives the maximum decomposition temperature T_m of 1085 K or 812 °C (in a strictly regular approximation, $T_m = Q/4$). Taking into account the dimension parameter $\Delta R/R_1 = 0.037$, the solvus deformation and the critical decomposition temperature in the approximation of an asymmetric solution are 48 mol.% MSO_4 and 780 °C, respectively. The miscibility diagram plotted using these data is shown in Figure 15 along with the experimental data. It can be seen that the experimental solvus is strongly shifted relative to the calculated one towards SO_4, and the points on its "sulfide" branch are in a poor agreement with the theoretical parabola.

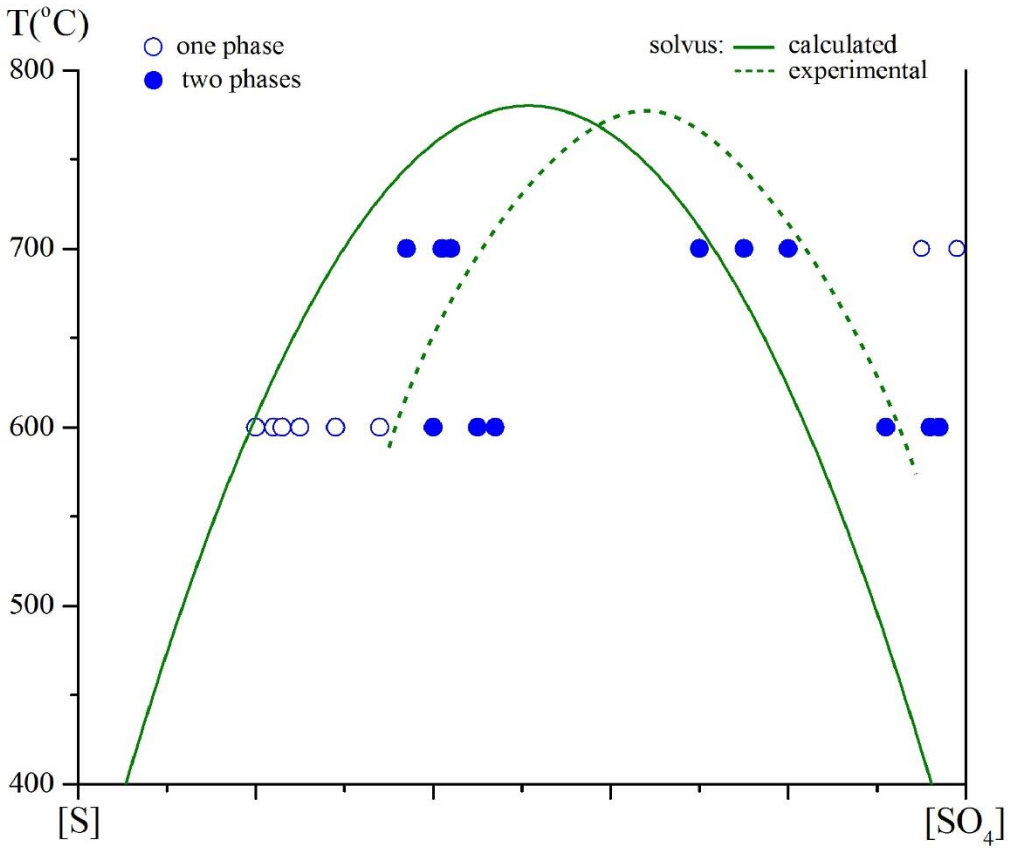

Figure 15. Calculated miscibility diagram in the Ca-bearing S-sodalite–haüyne system and experimental data.

Two factors can significantly affect the experimental results: the time of the experiment and the conversion of sulfur into various forms. The experiments at 800 °C on the annealing of sulfide-bearing haüyne (Sample 5) and vladimirivanovite (Sample 7) (see Table 9 in [68]) show that the latter factor plays a significant role and that this system cannot be considered as a quasi-binary one. According to XPS data, sulfur is present not only in sulfate form, but also in sulfite, thiosulfate and polysulfide forms. Thus, this diagram should be built in three dimensions, and the third axis should be the activity (volatility) of SO_2 [80]. The failure to take this circumstance into account complicates the use of sodalite-group minerals containing both sulfide and sulfate sulfur for geothermometric purposes. This applies, in particular, to the sodalite–nosean solvus [85], which, despite the critical temperature close to that obtained by us (~770 °C), is strongly deformed. This fact can be explained by the presence of various forms of sulfur in both coexisting phases (S-bearing sodalite and nosean) rather than the nonideality of the solid solutions.

3.4. Extra-Framework Components in Tugtupite

Tugtupite (Sample 8), when irradiated with ultraviolet light with a wavelength shorter than 450 nm, acquires a purple color. The purple color is associated with the appearance of an intense absorption band with a maximum of about 520 nm (Figure 16). When tugtupite is illuminated with light and the wavelength is in the range of 500–600 nm, the absorption band responsible for the purple color disappears. This is the cause of the color fading of this mineral in sunlight.

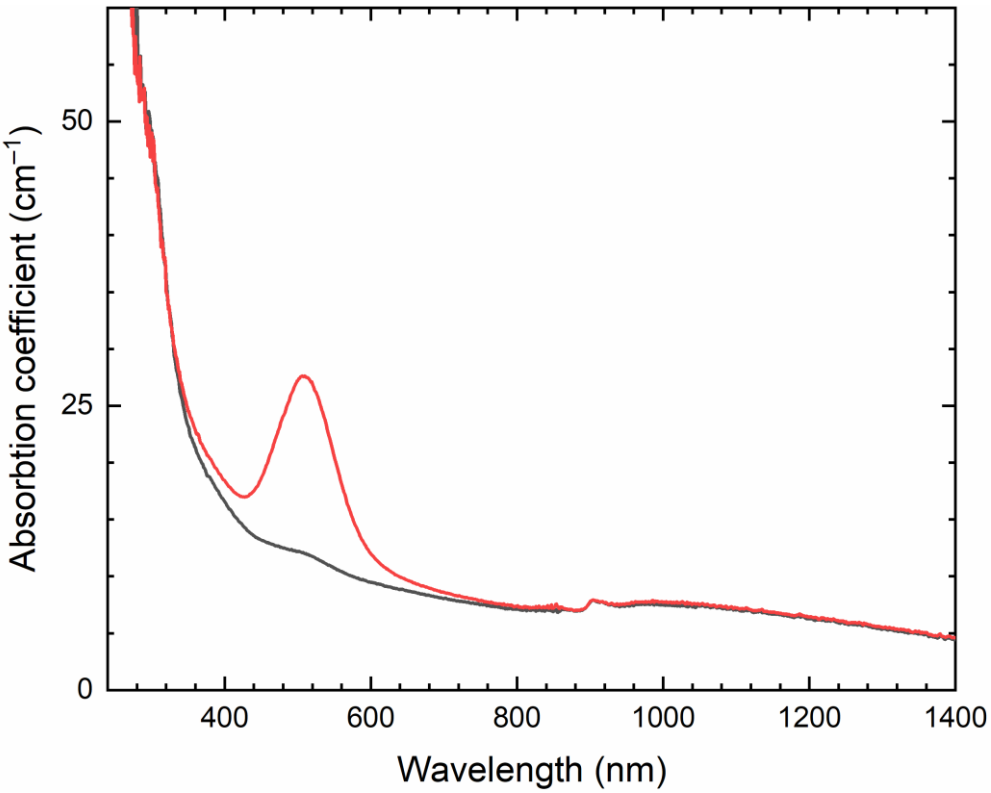

Figure 16. Absorption spectrum of tugtupite (Sample 8): almost colorless (black curve) and purple after irradiation with UV light (red curve).

Along with the appearance of a band in the region of 520 nm in the absorption spectrum, an intense ESR signal appears in the UV-irradiated tugtupite samples (in Figure 17, its components are marked with asterisks). As the color intensity increased, the intensity of these components also increased. After bleaching, the intensity of this signal significantly decreased. In addition, a signal with the g tensor components $g_1 = 2.210$; $g_2 = 2.010$; and $g_3 = 1.995$ related to the $S_2^{\bullet-}$ radical anions as well as a sextet with $g = 2.005$ corresponding to the Mn^{2+} cations, which was observed in the ESR spectra of tugtupite both before and after the irradiation. Earlier, similar signals were observed in the ESR spectra of other sodalite-group minerals [12,13].

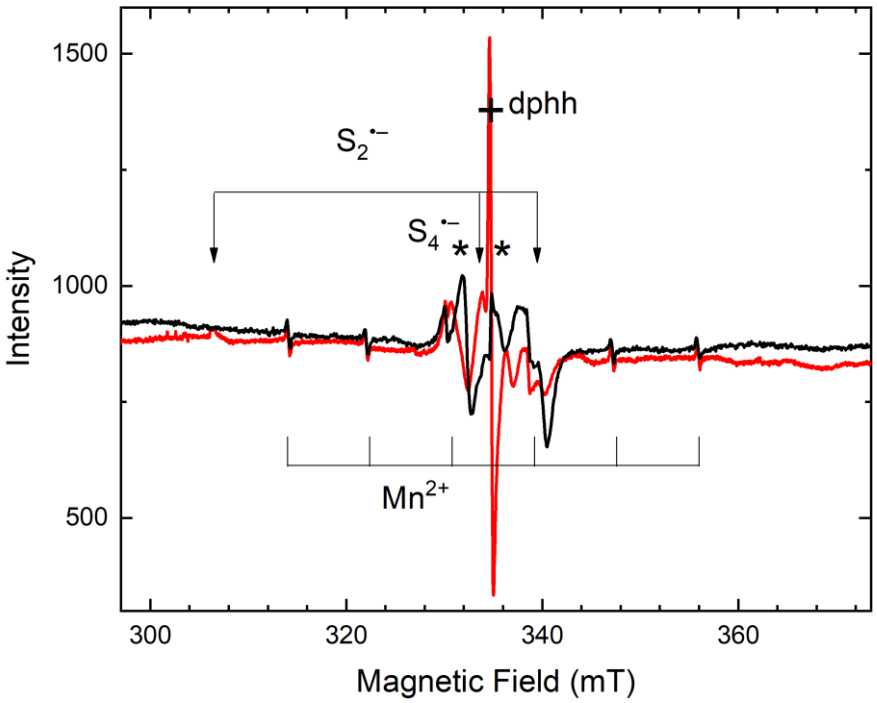

Figure 17. ESR spectra of purple tugtupite (Sample 8 irradiated by UV light, black curve) and almost colorless tugtupite (initially purple sample irradiated by light with the wavelength of 532 nm, red curve).

The presence of $S_2^{\bullet-}$ radical anions in the tugtupite is also confirmed by the presence of luminescence upon excitation with a light having a wavelength of about 400 nm. The luminescence spectrum (Figure 18) shows a band in the range of 600–800 nm, which has a pronounced vibrational structure with a phonon repetition frequency of about 520 cm^{-1} [86]. The luminescence excitation spectrum shows an intense band with a maximum at 390 nm. Such a luminescence is characteristic of the $S_2^{\bullet-}$ radical anions. For example, the luminescence maximum of sapozhnikovite, associated with the $S_2^{\bullet-}$ radical anions, was observed in the region of 625 nm with a phonon repetition frequency of 536 cm^{-1} [7]. The luminescence maximum of haüyne is about 650 nm, with a phonon repetition frequency of 690 cm^{-1} [5]. For hackmanite, the luminescence maximum is observed at 610 nm, and the phonon repetition frequency is 535 cm^{-1} [87].

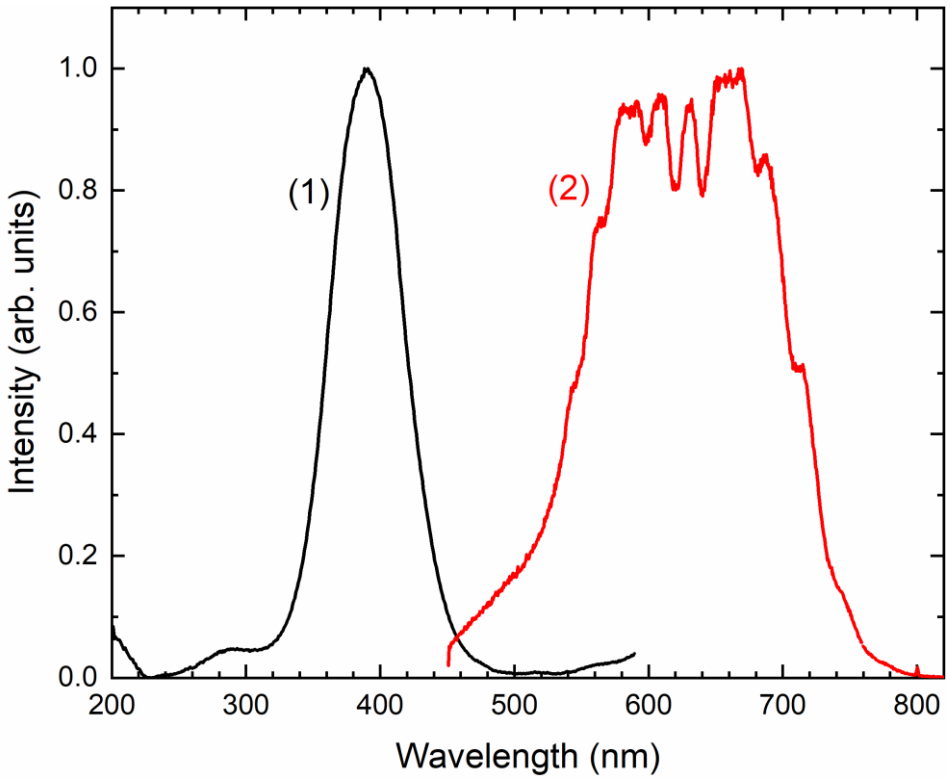

Figure 18. Excitation spectrum of tugtupite monitored at 605 nm (curve 1) and luminescence spectrum of tugtupite monitored at 400 nm (curve 2).

The phenomenon of photochromism (color change under the influence of light of different wavelengths) for the tugtupite has not been fully studied. There is no consensus on the nature of this phenomenon [88]. At first glance, the nature of the photochromism in the tugtupite is the same as in hackmanite, where the phototransfer of an electron from S_2^{2-} to a chlorine vacancy occurs upon UV irradiation. The resulting F_{Cl}^- centers (chlorine vacancy that captured an electron) have absorption bands in the vicinity of 550 nm [89]. A similar point of view is shared by the authors of other works [90,91]. However, the authors of [91] noted that when tugtupite is heated above 700 °C, photochromism disappears and the samples cease to turn purple, but they still exhibit the intense photoluminescence associated with $S_2^{\bullet-}$. This does not happen with hackmanite. Moreover, in some cases, after heating hackmanite, photochromism becomes more pronounced [13,91]. In addition, in the absorption spectrum of hackmanite, as a result of the ultraviolet coloration, the intensity of the shoulder at 400 nm increases, which is associated with an increase in the amount of $S_2^{\bullet-}$ radical anions as a result of the reaction $S_2^{2-} + \square_{Cl} \rightarrow S_2^{\bullet-} + F_{Cl}^-$, where □ is a vacancy. Along with the appearance of color, the EPR signal associated with the $S_2^{\bullet-}$ radical anions increases [90]. This does not take place in the case of tugtupite.

Thus, the nature of photochromism in the case of tugtupite may differ from that of hackmanite. In the ESR spectrum of the irradiated tugtupite, which has a saturated purple color, an ESR signal with $g_1 = 2.020$ and $g_2 = 2.001$ is observed. This signal was previously observed in the ESR spectra of the minerals of the sodalite and cancrinite groups and was attributed to the $S_4^{\bullet-}$ radical anions [12,13]. Moreover, such radical anions have absorption bands in the region of 500–540 nm, and samples containing $S_4^{\bullet-}$ and $S_2^{\bullet-}$ radical anions have a color close to that of tugtupite [13]. During heating, the decomposition of the $S_4^{\bullet-}$ radical anions occurs with a simultaneous increase in the concentration of $S_2^{\bullet-}$ [13]. This explains the disappearance of photochromism in the heated samples of tugtupite.

3.5. Extra-Framework Components in Vladimirivanovite and their Thermal Transformations

In the absorption spectrum of vladimirivanovite (Sample 7, Figure 19), there is an intense broad table-like band in the range of 465–850 nm with a small step in the region of 505 nm and a weak band with a maximum at 930 nm. The edge absorption starts below 430 nm. The observed absorption spectrum is characteristic of the previously studied haüyne samples [5,12].

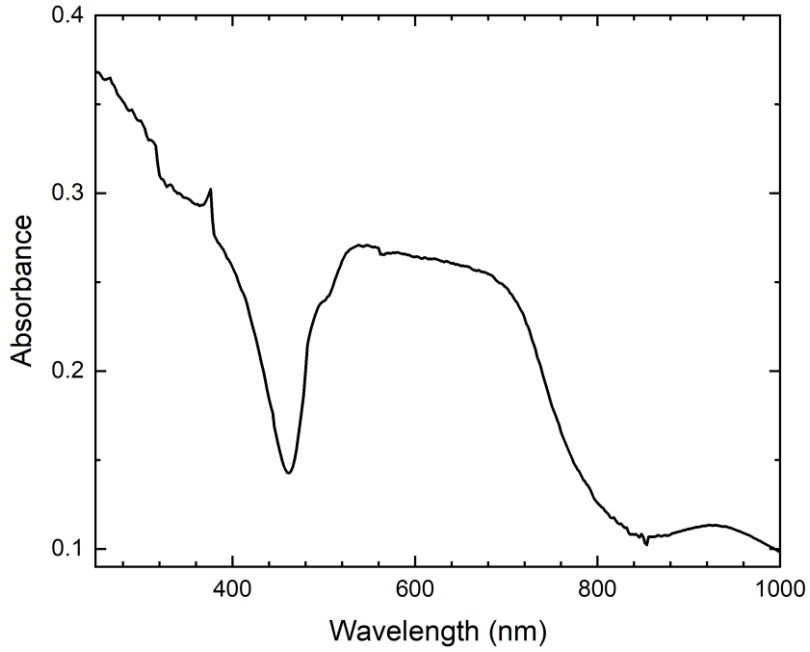

Figure 19. The absorption spectrum of vladimirivanovite (Sample 7).

The ESR spectrum of vladimirivanovite (Figure 20) shows an intense signal c g_1 = 2.049, g_2 = 2.038 and g_3 = 2.011. This signal is associated with the presence of the $S_3^{\bullet-}$ radical anions. The same species cause an absorption in the region of 465–850 nm. Based on the values of the components of the g tensor, we can conclude that the geometry of the $S_3^{\bullet-}$ radical anion is close to $S_3^{\bullet-}$ in haüyne.

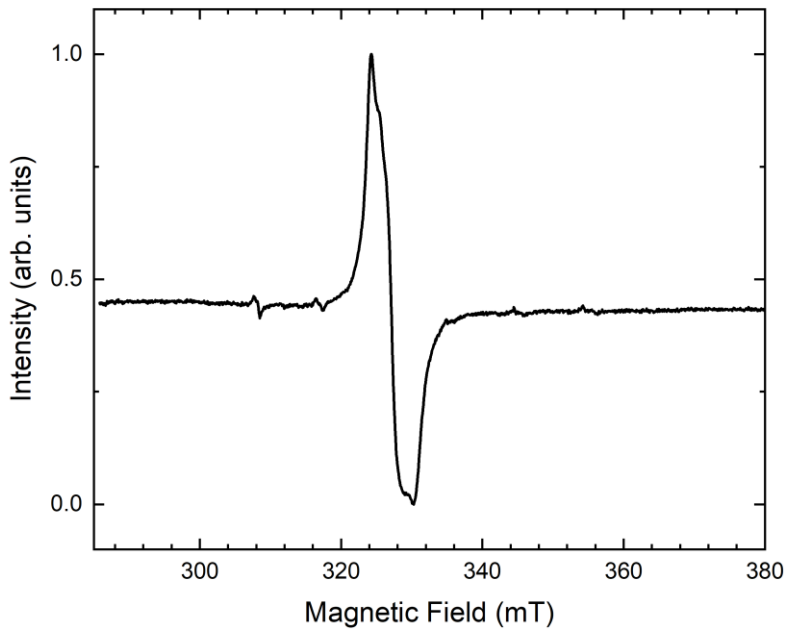

Figure 20. The ESR spectrum of vladimirivanovite (Sample 7).

The ESR spectrum of vladimirivanovite also shows a band with g = 2.021 (Figure 20). This ESR signal is characteristic of the $S_4^{\bullet-}$ radical anion, and this is confirmed both by the presence of a step in the region of 505 nm and by a weak band at 930 nm [13].

When vladimirivanovite is heated above 600 °C, the intensity of the absorption band in the region of 480–850 nm increases, and the step in the absorption spectrum and the ESR signal with g = 2.021 disappears. This is due to the fact that the $S_4^{\bullet-}$ radical anions are unstable upon heating and transform into $S_3^{\bullet-}$ [13].

3.6. S-Bearing Groups in Biachellaite and SO_3^{2-}-Rich Analogue of Marinellite

The Raman spectra of biachellaite (Sample 14) and SO_3^{2-}-bearing analogue of marinellite (Sample 13a) are presented in Figure 21. Both samples show a strong luminescence under the laser beam. The bands in the ranges of 1090–1170, 989–992, 614–640 and 436–458 cm^{-1} correspond to the vibrations of the SO_4^{2-} anions (the $F_2(\nu_3)$, $A_1(\nu_1)$, $F_2(\nu_4)$ and $E(\nu_2)$ modes, respectively). The additional bands at 1037, 965 and 678 cm^{-1} observed in the Raman spectrum of the SO_3^{2-}-bearing analogue of marinellite as well as the splitting of the band in the range of 436–458 cm^{-1} are due to the presence of the SO_3^{2-} anions. Analogous bands in the Raman spectrum of hannebachite, $Ca(SO_3)\cdot 0.5H_2O$, observed at 1005, 969 and 655 cm^{-1} and in the range of 444–520 cm^{-1} have been assigned to the $A_1(\nu_1)$, $E(\nu_3)$, $A_1(\nu_2)$ and $E(\nu_4)$ modes, respectively [71]. However, some components of a triplet observed in the Raman spectrum of hannebachite in the range of 444–520 cm^{-1} may correspond to resonance modes involving the H_2O liberation. Similarly, the doublet 436 + 458 cm^{-1} in the Raman spectrum of Sample 13a may be due to a resonance between the $E(\nu_2)$ and $E(\nu_4)$ modes and the SO_4^{2-} and SO_3^{2-} anions occurring in the liottite cage.

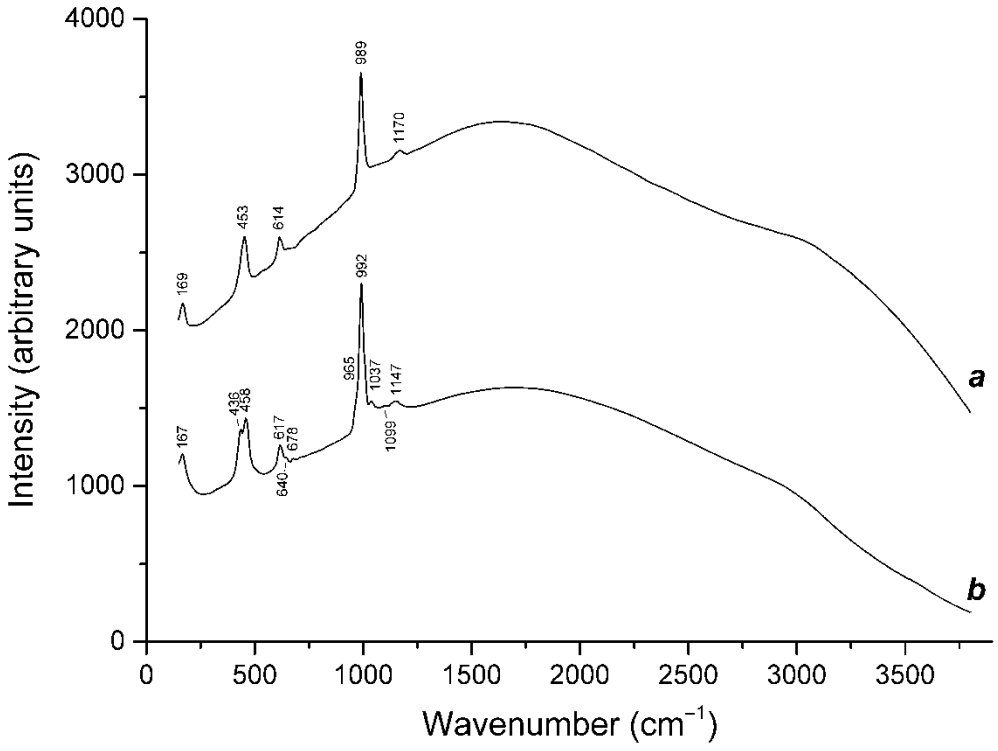

Figure 21. Raman spectra of (**a**) biachellaite (Sample 14) and (**b**) SO_3^{2-}-bearing analogue of marinellite (Sample 13a).

Marinelite has a bluish-violet color due to the presence of an absorption band with a maximum at ~580 nm (Figure 22). The absorption spectrum also shows an increase in the absorption towards the short wavelength, starting from 400 nm. When excited by radiation with a wavelength of about 400 nm, marinellite exhibits an orange–red luminescence with a maximum at 580 nm, which has a characteristic vibrational structure with phonon

repetitions at a distance of 535 cm^{-1}. The ESR spectrum of marinellite (Figure 23) shows a signal with g_1 = 2.220 and g_2 = 2.007. This signal and luminescence are associated with the presence of $S_2^{\bullet-}$ radical anions in marinellite (see [92]). Additionally, an intense signal with g = 2.019 is observed in the ESR spectrum. The presence of this EPR signal and the absorption band at 580 nm may indicate the presence in marinellite of $S_3^{\bullet-}$ radical anions, the point symmetry group which is close to D_{3h}, i.e., the sulfur ions form a three-fold ring close to a regular one [92–94]. Usually, such a configuration of the $S_3^{\bullet-}$ radical anion is not realized in the minerals.

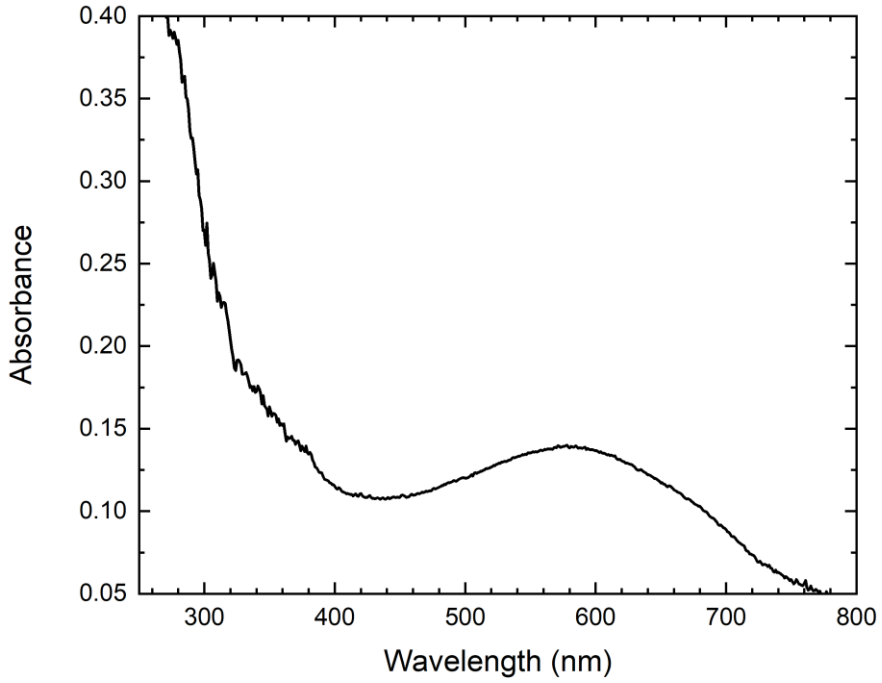

Figure 22. Absorption spectrum of the SO_3^{2-}-bearing analogue of marinellite (a mixture of Sample 13a and Sample 13b).

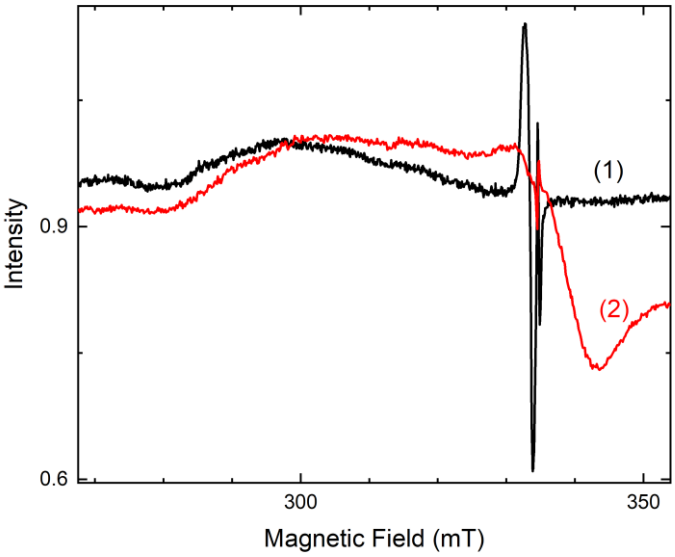

Figure 23. ESR spectra of biachellaite (Sample 14, curve 1) and marinellite sulfite analogue (curve 2).

The sample of biachellaite (Sample 14), when excited by a radiation with a wavelength of 405 nm, also shows a pinkish luminescence with a maximum of about 620 nm and a characteristic vibrational structure, where the phonon repetition frequency is about

500 cm^{-1} (Figure 24). The ESR spectrum of biachellaite (Figure 24) shows a signal with the *g*-tensor components of 2.20, 2.02 and 1.99. This ESR signal and the observed pinkish luminescence can be attributed to the $S_3^{\bullet-}$ radical anions [94].

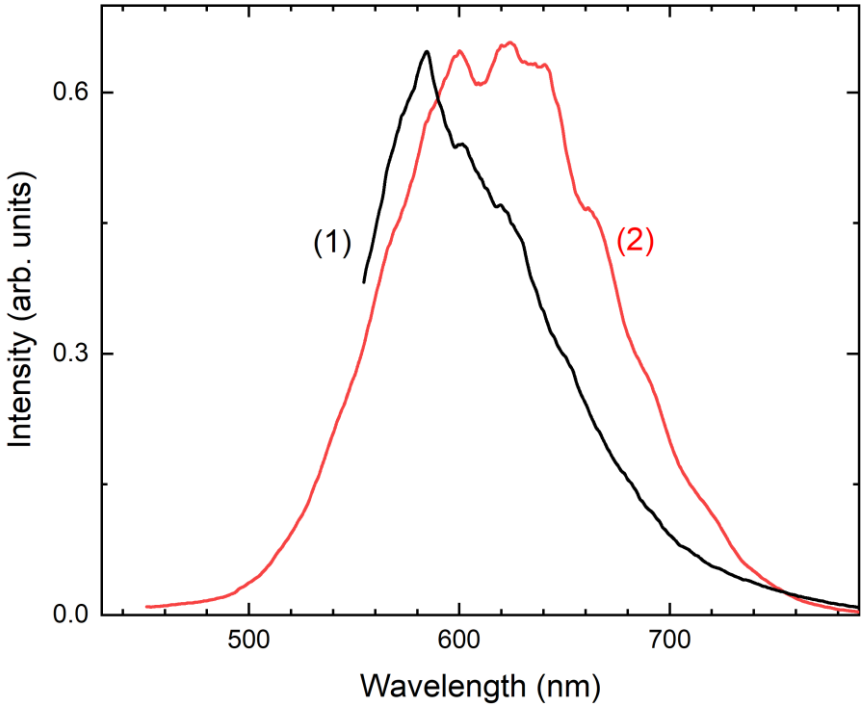

Figure 24. Emission spectra of marinellite (1) and biachellaite (2) upon excitation by radiation with a wavelength of 405 nm.

3.7. S-Bearing Scapolites

The assignment of the Raman bands of the SO_4^{2-}-rich meionite (Sample 15, Figure 25) is as follows. The peaks at 1102 and 1500 cm^{-1} correspond to the symmetric and asymmetric stretching modes of the CO_3^{2-} anions, respectively. The bands at 986 and 1038 cm^{-1} are due to the symmetric and asymmetric stretching modes of the SO_4^{2-} anions, respectively. SO_4^{2-} bending modes correspond to the peaks at 416, 584 and 648 cm^{-1}. Other bands in the range of 400–800 cm^{-1} are due to the vibrations of the aluminosilicate framework. The bands of the lattice modes involving translational and rotational vibrations of the extra-framework components are observed below 400 cm^{-1}.

Weak bands above 1700 cm^{-1} could not be assigned to any overtones or combination modes. Presumably, these bands correspond to extremely strong hydrogen bonds in local situations with H_3O^+ at the Ca^{2+}-dominant site and H_2O at the CO_3^{2-}-dominant site, which would result in the formation of Zundel cation, $H_5O_2^+$, by analogy with the nosean [12].

In the Raman spectrum of the SO_4^{2-}-poor meionite (Sample 16, Figure 25) bands, the SO_4^{2-} groups are relatively week and the bands of presumed strong hydrogen bonds corresponding to a hydrated proton complex (in the range of 1190–3300 cm^{-1} [76]) are stronger than the analogous bands of Sample 15.

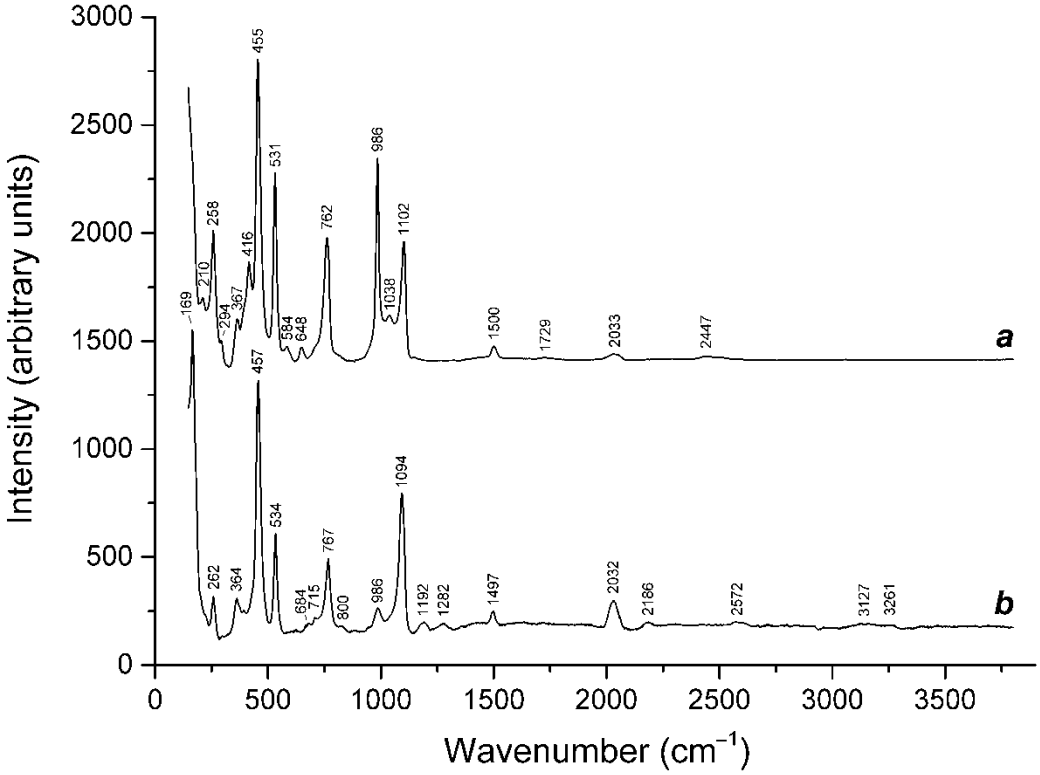

Figure 25. Raman spectra of (**a**) SO_4^{2-}-rich meionite (Sample 15) and (**b**) SO_4^{2-}-poor meionite (Sample 16).

As a rule, the Raman band of the symmetric stretching vibrations of the carbonate anion is observed in the range of 1040–1100 cm^{-1} (usually from 1060 to 1090 cm^{-1}). Among several hundred carbonate minerals, few exceptions are several magnesium carbonates, two uranyl carbonates (kamotoite and rutherfordine) and tunisite, for which this band is shifted to higher frequencies [95]. Thus, the band at 1102 cm^{-1} in the Raman band of Sample 15 can be considered as an anomaly, which may be caused by steric hindrances, which may increase with the enhancement of the content of the sulfate groups in the mineral.

3.8. Synthesis and Thermal Conversions of S-Bearing Sodalite- and Cancrinite-Type Materials

Figure 26 illustrates the morphological features of the aggregates of the products of synthesis. The chemical data (Table 5), unit cell parameters (Table 4) and Raman spectrum (curve 1 in Figure 27) of the powder obtained in Experiment 1, correspond to sapozhnikovite $Na_8[Al_6Si_6O_{24}](HS)_2$, a newly described member of the sodalite group [7]. In particular, the Raman bands at 260, 455, 996 and 2666 cm^{-1} correspond to the bending vibrations of the $[(HS)Na_4]^{3+}$ cluster, stretching the vibrations of the $[(HS)Na_4]^{3+}$ cluster, a stretching mode of the aluminosilicate framework and stretching vibrations of the HS^- anion. The broad Raman bands of this sample may correspond to an admixed X-ray amorphous phase. This is the first example of the synthesis of a HS-bearing sodalite-type compound. The synthetic analogue of sapozhnikovite occurs as tiny rhombic dodecahedral crystals up to 9 μm across (Figure 26a).

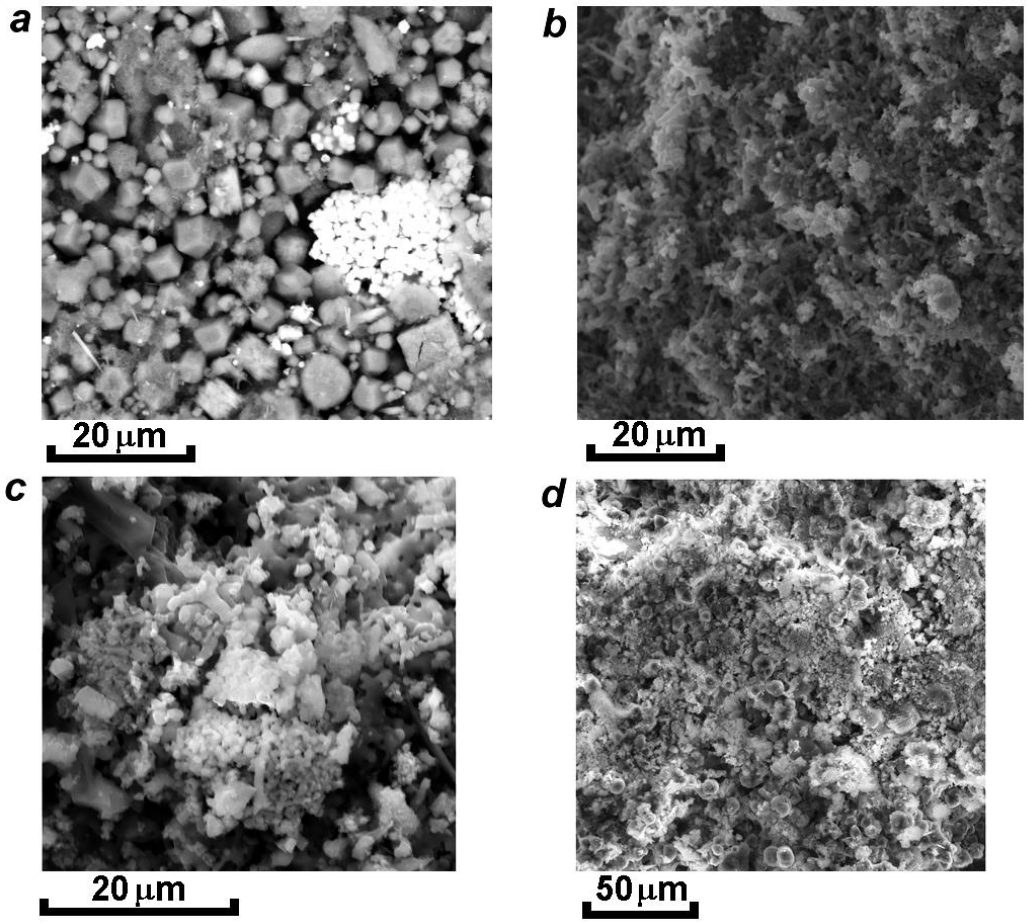

Figure 26. Aggregates of (**a**) synthetic analogue of sapozhnikovite obtained in Experiment 1, (**b**) intimate intergrowth of sodalite- and cancrinite-type phases mixture from Experiment 2, (**c**) product of Experiment 2a and (**d**) cancrinite-type phase from the Experiment 6. SEM photos obtained in the BSE (**a**) and SE (**b**–**d**) modes.

The heating of the synthetic analogue of sapozhnikovite under oxidizing conditions (Experiment 1a) resulted in the disappearance of the HS^- anion and the formation of the SO_4^{2-} group. In particular, the Raman bands at 433, 616, 980 and 1130 cm^{-1} belong to the bending and stretching modes of SO_4 tetrahedron [5,8,12,13]. The bands at 311–336 and 1341 cm^{-1} can be interpreted as mixed and antisymmetric $2\nu_3$ modes of the *cis*-S_4 molecule, respectively. The band at 2159 corresponds to an acid group, presumably HSO_4^-.

The Raman spectrum of the synthetic sapozhnikovite analogue treated under reducing conditions (Experiment 1b) demonstrates the presence of SO_4^{2-} and $S_3^{\bullet-}$ that are the most stable S-bearing groups at temperatures above 800 °C. The band at 976 cm^{-1} is due to the symmetric vibrations of the sulfate anions, whereas the bands at 254 cm^{-1} (bending ν_2 mode), 544 cm^{-1} (symmetric stretching ν_1 mode), 802 cm^{-1} (combination mode $\nu_1 + \nu_2$), 1091 cm^{-1} (overtone $2'\nu_1$), 1640 cm^{-1} (overtone $3 \times \nu_1$) and multiple bands above 1500 cm^{-1} (different combination modes and overtones) correspond to $S_3^{\bullet-}$ [5,8,12,13]. The weak bands at 673 and 1337 cm^{-1} correspond to the *trans*-S_4 symmetric stretching ν_3 mode and its first overtone, respectively. The band at 589 cm^{-1} may be due to the stretching vibrations of the $[(S^{2-})Na_4]^{2+}$ cluster. Thus, the product of Experiment 1b is close to the minerals belonging to the lazurite-haüyne solid-solution series described by us earlier [5,8,12,13]. The presence of significant amounts of the $S_3^{\bullet-}$ radical anions in the product of Experiment 1b determines the deep blue color of its powder.

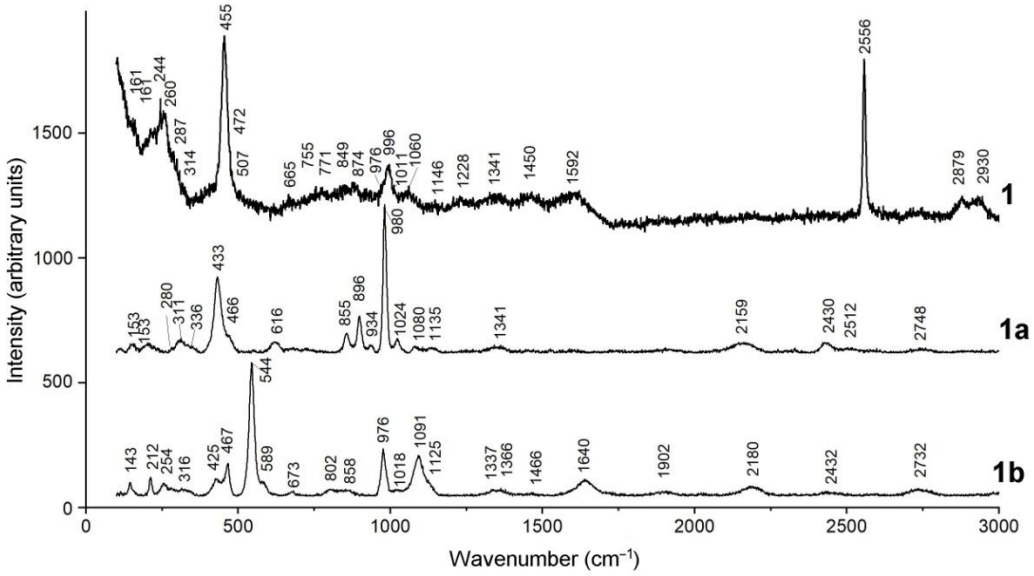

Figure 27. Raman spectra of powders obtained in Experiments 1, 1a and 1b. The description of the experimental conditions is given in Table 4.

The transformation of the HS^- anion in the β-cage in the crystal structure of the synthetic analogue of sapozhnikovite during heating and the formation of the large sulfate group results in a phase transition accompanied by a significant expansion of the framework and, respectively, in the enhancement of the unit cell parameter (Table 4). The powder X-ray diffraction patterns of the products of Experiments 1, 1a and 1b are shown in Figure 28. The crystal structure of the initial sample corresponds to the space group *P*-43*n*. The strong reflections [100] and [300] which appeared in the XRD patterns of the products of Experiments 1a and 1b and indicate the space group *P*23, correspond to a sodalite-type structure with ordered $[Na_4X]^{2+-3+}$ and $[Na_4(H_2O)]^{4+}$ clusters, where *X* is an anion [96,97]. The heating of the studied compounds can result in both a water release and the transformation of the S-bearing groups. This causes changes in the composition of the extra-framework components and their redistribution, which may result in the commensurate and incommensurate modulations of the crystal structure [5,6].

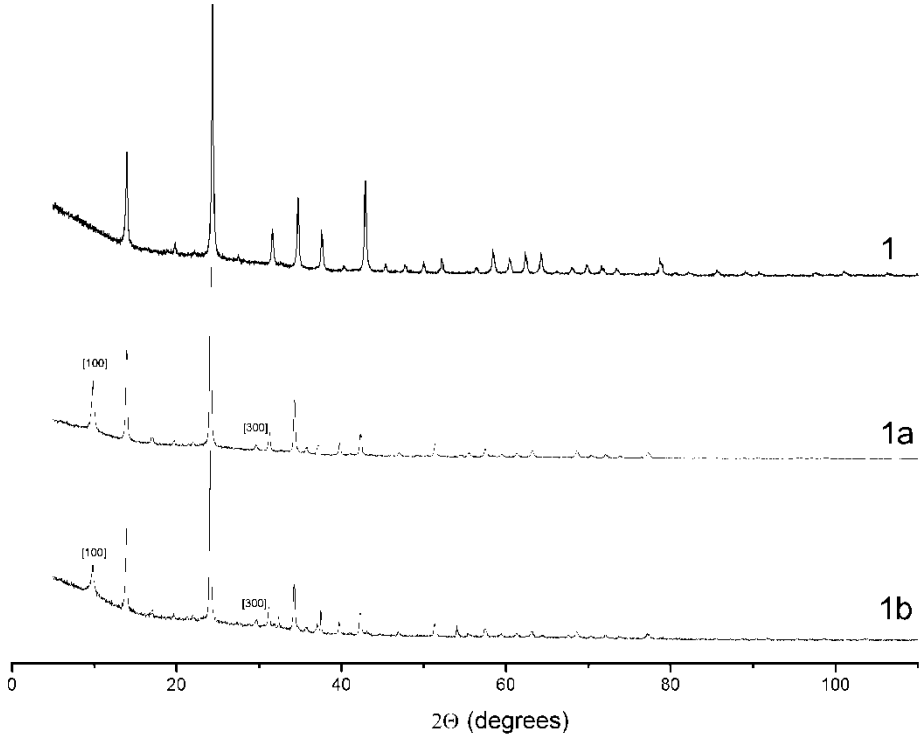

Figure 28. Powder X-ray diffraction patterns of the products of Experiments 1, 1a and 1b. All reflections correspond to sodalite-type phases [the space groups *P*-43*n* (Experiment 1) and *P*23 (Experiments 1a and 1b)]. The reflections [100] and [300] are marked as indicative for *P*23 space group.

The product of Experiment 2 with the $Na_2SO_3 \cdot 5H_2O$ salt contains both sodalite- and cancrinite-type compounds (Figures 28 and 29, Table 4). Presumably, the cancrinite-type phase occurs as tiny elongate crystals in a matrix of a fine-grained aggregate containing a sodalite-type compound. The strongest band at 1077 cm^{-1} observed in the Raman spectrum of this material corresponds to the symmetric stretching vibrations of the CO_3^{2-} anion that does not belong to a cancrinite-type phase or a sodium carbonate. Thus, the carbonate group occurs in the sodalite-type phase. The bands at 991 and 968 cm^{-1} as well as 674 and (partly) 450 cm^{-1} may be due to the stretching and bending vibrations of a minor admixture of the SO_3^{2-} anions. The band at 1331 cm^{-1} may correspond to a Fermi resonance mode of the CO_2 molecules involved in strong dipole–dipole interactions. The remaining (weak) bands in the ranges of 100–400, 600–900 and 1200–3000 cm^{-1} correspond to soft lattice modes, the framework vibrations and the O–H stretching vibrations of the Zundel cation, $H_5O_2^+$, respectively. Both the chemical composition and the Raman spectrum of the product of Experiment 2a correspond to the Na-deficient nosean (Table 4, Figure 29). In this reference, it is to be noted that the partial substitution of Na^+, belonging to the $Na_4 \cdot H_2O$ cluster with the Na···O distance of 2.6 Å in the nosean structure, with hydronium results in the formation of the Zundel cation [12].

A very small *a* parameter of the sodalite-type phase (8.8867 Å) indicates that a major part of the sulfur belongs to a very small anion (presumably, S^{2-}) rather than SO_3^{2-} or SO_4^{2-}. According to the local microanalysis of the chemical composition, sulfur occurs only in the cancrinite-type phase, whereas S-bearing species are absent in the fine-grained aggregates containing a sodalite-type phase.

The initial sample is a mixture of the sulfite analogue of Ca-free cancrinite (space group $P6_3$) with a subordinate S-free sodalite-type phase. The powder X-ray diffraction data show that a thermal treatment results in the transition of the cancrinite-type phase to a compound with the sodalite-type structure (Figure 30). The heating of this sample under oxidizing conditions results in the decomposition of the carbonate groups and ap-

pearance of a full set of bands corresponding to fundamentals of the SO_4^{2-} anion (the peaks at 427, 615, 978, 1079 and 1130 cm^{-1}). The sulfate groups remain stable during heating under reducing conditions at 700 °C (Experiment 2b; see Figure 29). In the annealed samples (Experiments 2a and 2b), the main phase belongs to the sodalite type with space group *P*23 as in Experiments 1a and 1b. This transformation is accompanied by the enhancement of the unit cell parameter of the sodalite-type phase from 8.8867 Å to 9.0928 Å (Table 4). The structural transition can be due to the stabilizing effect of SO_4^{2-} and, to a lesser extent, SO_3^{2-} on the sodalite-type crystal structure at high temperatures. The impurity phase detected in Experiments 2a and 2b is a synthetic analogue of nepheline (Figure 30).

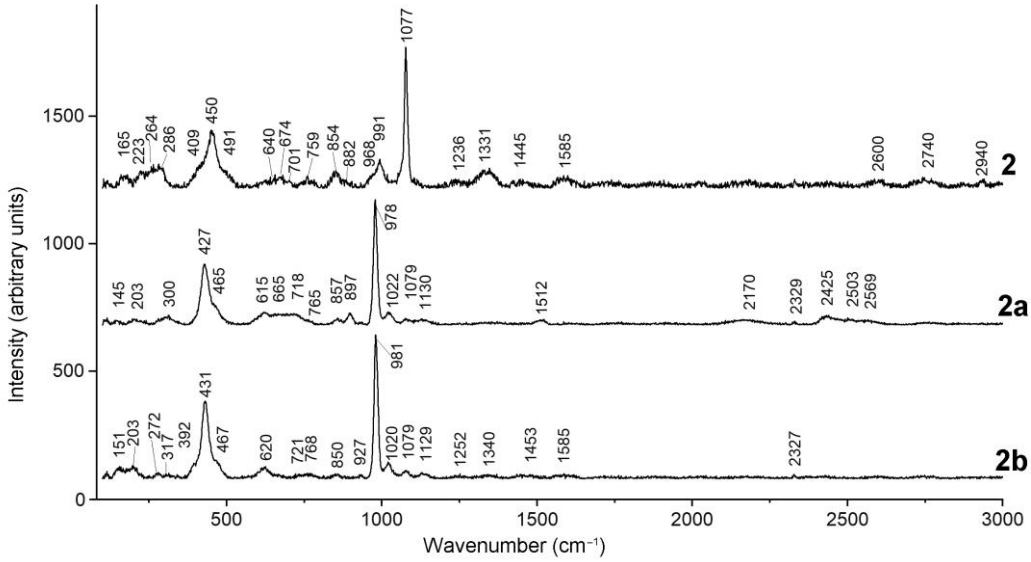

Figure 29. Raman spectra of the products of the Experiments 2, 2a and 2b.

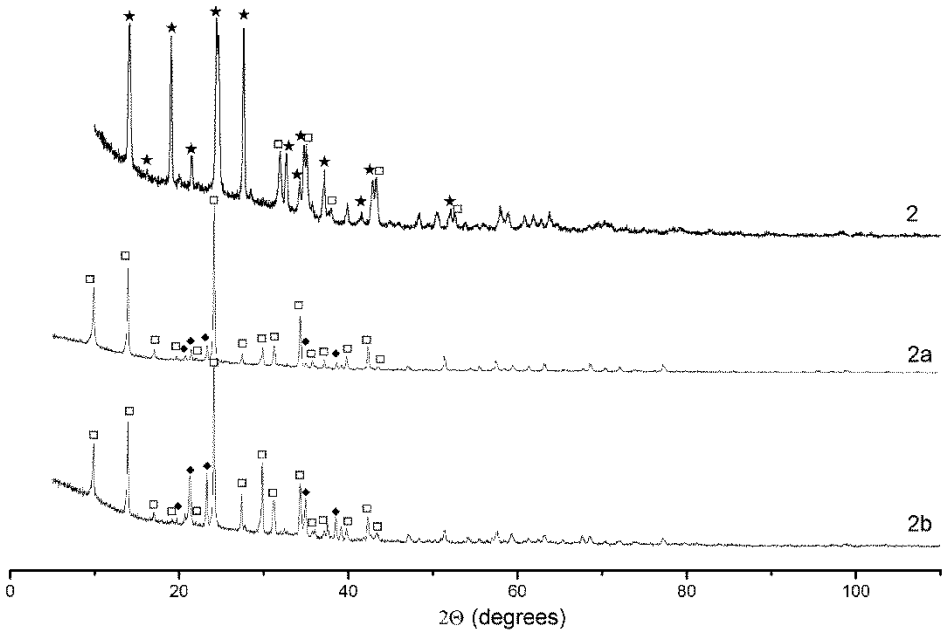

Figure 30. Powder X-ray diffraction patterns of the products of Experiments 2, 2a and 2b. The characteristic non-overlapping reflections of cancrinite-type (□), sodalite-type (★) and nepheline-type (◆) phases are indicated.

According to the chemical, powder X-ray diffraction and Raman spectroscopy data (Figures 31 and 32, Tables 4 and 5), the main phase in the product of Experiment 3 is a cancrinite-type compound with the thiosulfate group as the dominating extra-framework anion. In the Raman spectrum (Figure 31), a set of characteristic bands of the $S_2O_3^{2-}$ anion is observed: the strongest band at 449 cm^{-1} corresponds to the S–S stretching A1 mode; the bands at 995, 1135 and 1079 cm^{-1} are due to the symmetric, asymmetric and mixed S–O stretching modes, respectively. The bands at 543 and 664 cm^{-1} correspond to the O–S–O bending modes. The assignment of the Raman bands of $S_2O_3^{2-}$ was made using data from [98–103].

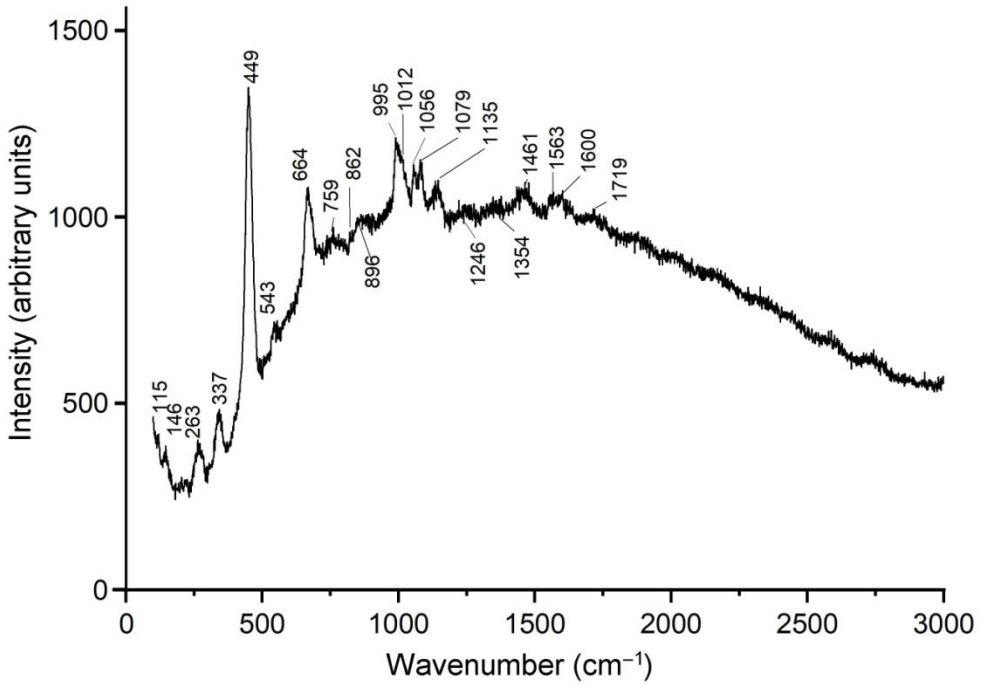

Figure 31. Raman spectrum of the product of Experiment 3.

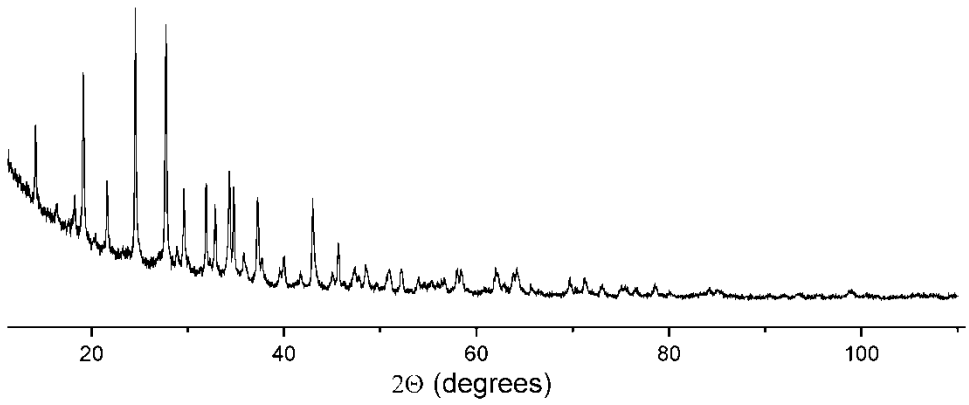

Figure 32. Powder X-ray diffraction pattern of the product of Experiment 3. All reflections correspond to a cancrinite-type phase.

4. Discussion

4.1. General Remarks on the Isomorphism of S-bearing Species in Feldspathoids

All available data on the crystal structures of S-bearing feldspathoids show that among acyclic polysulfide groups, S_n, S_n^{2-} and $S_n^{\bullet-}$, only species with an $n < 5$ can occur in sodalite cages. The presence of the cyclic S_6 molecule in slyudyankaite, a mineral with the

sodalite framework topology, results in the symmetry lowering to the triclinic and regular alternation of S_6- and SO_4^{2-}-bearing sodalite cages. The acyclic S_5^{2-} anion is known only in the Losod cages of minerals belonging to the bystrite–sulfhydrylbystrite solid-solution series, for which the presence of variable amounts of the HS^- anion is typical. Except bystrite-type minerals, the HS^- anion is known in sapozhnikovite [7] and the products of the heating of other S-bearing sodalite-group minerals under strongly reducing conditions (over the Fe-FeS buffer) [13]. Based on these facts and taking into account the occurrence of sapozhnihovite in a close association with the oxalate member of the cancrinite group kianoxalite, one can conclude that the HS^- and S_5^{2-} anions can be considered as the markers of extremely reducing conditions. Moderately reducing conditions contribute to the formation of the sulfite analogues of cancrinite-group minerals, including the SO_3^{2-}-bearing analogue of marinellite described in this paper and sulfite minerals with the afghanite-type framework described elsewhere [9,103,104].

4.2. Structural Relationships between S-Bearing Sodalite-Group Minerals

Some chemical and structural data for S-bearing minerals with the sodalite-type framework topology are given in Table 7. As one can see from these data, minerals with the lowest (<1.4 wt.%) and highest (>4 wt.%) contents of sulfide sulfur are cubic, whereas minerals with intermediate contents of sulfide sulfur have a lower symmetry. The simultaneous presence of high amounts of sulfate anion, trisulfide radical anion or cyclic hexasulfide molecule in a sodalite-group mineral results in a commensurate and/or incommensurate modulation of the crystal structure that may be due to differences in the sizes of sodalite cages hosting large SO_4^{2-}, $S_3^{\bullet-}$ or S_6 groups. Significant amounts of these groups are present in the structures of all S-bearing minerals with the sodalite-type framework topology, except sapozhnikovite. As a result, sapozhnnikovite has a low unit cell a parameter (<8.92 Å), whereas the a parameter of other S-bearing sodalite-group minerals is in the ranges of 9.05–9.12 Å.

The symmetry lowering in the minerals with intermediate contents of sulfide sulfur may be due to the different sizes of the sodalite cages hosting sulfate and sulfide groups that results in strains and distortions of the framework. Hypothetically, in lazurite (a mineral with a cubic unit cell and the largest a parameter among the sulfide-bearing members of the sodalite group), the straining of the framework is small because of a partial ordering of SO_4^{2-} and $S_3^{\bullet-}$.

Table 7. Data on S-bearing sodalite-group minerals.

Mineral	SO_3, wt.% S *, wt.%	Kinds of Sulfide Groups	Symmetry	Unit Cell Parameters	References
Nosean	10.27 0	-	Cubic	a = 9.084(2) Å	[12,105]
Haüyne	14.2 0	-	Cubic	a = 9.1164(5) Å	[106]
SO_4^{2-}-deficient haüyne	12.43 0.11	**$S_2^{\bullet-}$**, $S_3^{\bullet-}$	Cubic **	a = 9.065(1) Å	[5]
S_4-bearing haüyne (Sample 5)	13.89 1.31	**S_4**, $S_3^{\bullet-}$	Cubic **	a = 9.071(2) Å	[5], this work
Slyudyankaite	10.95 1.75	**S_6**, S_4, $S_3^{\bullet-}$	Triclinic **	a = 9.0523(4) Å b = 12.8806(6) Å c = 25.681(1) Å α = 89.988(2)° β = 90.052(1)°	[107]

				γ = 90.221(1)°	
"Monoclinic lazurite"	10.89 1.94	**$S_3^{\bullet-}$**, S_4	Monoclinic **	a = 9.069(6) Å b = 12.868(1) Å c = 25.744(1) Å γ = 90.19(1) (1)°	[108,109], this work
Vladimirivanovite	11.37 1.94	**$S_3^{\bullet-}$**, $S_2^{\bullet-}$	Orthorhombic **	a = 9.066(2) Å b = 12.851(3) Å c = 38.558(8) Å	[64], this work
Sapozhnikovite	0 4.20	**HS^-**, $S_2^{\bullet-}$	Cubic	a = 8.91462(7) Å	[7]
Lazurite	8.08 5.07	**$S_3^{\bullet-}$**, S^{2-}	Cubic **	a = 9.087(2) Å	[6]

* Total content of sulfide sulfur. ** Structures with commensurate and/or incommensurate modulation. The main sulfide groups are indicated in bold type.

4.3. Thiosulfate Anion as an Extra-Framework Constituent of Cancrinite-Type Compounds

The thiosulfate analogues of cancrinite and sodalite are unknown in nature. The data on the first synthesis of the phase with the empirical formula $Na_{6.9}[Al_{5.6}Si_{6.4}O_{24}](S_2O_3)\cdot nH_2O$ shows that there is only one $S_2O_3^{2-}$ group per unit cell and the crystal structure of this phase has the space group *P*3 with the unit cell parameters a = 12.624(2) and c = 5.170(1) Å [102]. Our data on the thiosulfate cancrinite-type phase do not contradict the previous results on the crystal structure.

There are no data on the Raman spectroscopy of the thiosulfate anion as a constituent of sodalite- or cancrinite-type compounds. It is noteworthy that the frequencies of the $S_2O_3^{2-}$ modes determined for the synthetic thiosulfate cancrinite-type phase (Experiment 3) are quite close to those inherent to the free $S_2O_3^{2-}$ anion [100].

4.4. Thermal Transformations of S-Bearing Species in Feldspathoids

Preliminary experiments with the heating of S_4- and CO_2-bearing haüyne (Sample 5) have been described by us earlier [13]. It was shown that the main channel of the transformations of the extra-framework components at 700 °C under reducing conditions (in the presence of Fe-FeS buffer) is $SO_4^{2-} \rightarrow S^{2-} + 2O_2$(gas), and the subordinate processes are $CO_2 + 2SO_4^{2-} + H_2O \rightarrow 2HS^- + CO_3^{2-} + 4O_2$(gas), $3SO_4^{2-} \rightarrow S_3^{\bullet-} + 5e + 6O_2$(gas), $2S_3^{\bullet-} \rightarrow S_2^{\bullet-} + S_4^{\bullet-}$ and $2CO_2 + 2e \rightarrow C_2O_4^{2-}$ (e = electron). The annealing of the preheated samples in air at 800°C results in partial reverse transformations: $S_2^{\bullet-} + S^{2-} + 2O_2$(gas) $\rightarrow SO_4^{2-}$, $S_4^{\bullet-} + S_2^{\bullet-} \rightarrow 2S_3^{\bullet-}$, as well as subordinate processes $S_3^{\bullet-} + 5e + 6O_2$(gas) $\rightarrow 3SO_4^{2-}$ and $C_2O_4^{2-} \rightarrow 2CO_2$(gas) + 2$e$. These conclusions are in agreement with the Raman spectra shown in Figure 13.

Based on the Raman spectroscopy data, one can suppose that the main channel of the high-temperature transformations of the HS^- anion in the synthetic analogue of sapozhnikovite is $2HS^-$ (solid) + $2.5O_2$ (gas) $\rightarrow SO_4^{2-}$ (solid) + $0.25S_4$ (solid) + H_2O (gas). Hypothetically, the subordinate channels of the transformations of the HS^- anion during the heating of this sample under oxidizing and moderately reducing conditions can be described by the schemes $2HS^-$ (solid) + $3.5O_2$ (gas) $\rightarrow SO_4^{2-}$ (solid) + SO_2 (gas) + H_2O (gas) and $6HS^-$ (solid) $\rightarrow S_3^{\bullet-}$ (solid) + $3H_2S$ (gas), respectively.

4.5. Color Centers in Feldspathoids and Related Minerals

The only strong red chromophore among the tetrasulfur species is the planar non-cyclic C_{2v} isomer of the neutral S_4 molecule [47]. As noted above, all strong bands of this molecule are present in the Raman spectrum of orange sulfhydrylbystrite, unlike yellow bystrite. Thus, it can be concluded that the color of the bystrite and sulfhydrylbystrite is due to the presence of S_5^{2-} (yellow chromophore) and the pair $S_5^{2-} + S_4$, respectively.

Undistorted $S_3^{\bullet-}$ radical anions are the cause of the blue color of kyanoxalite and different sodalite-group minerals, including lazurite, haüyne and vladimirivanovite. The bluish-violet color of the sulfite analogue of marinellite is unusual for cancrinite-group minerals. The ESR spectrum of this mineral shows the presence of distorted $S_3^{\bullet-}$ radical anions (with a lowered S–S–S angle), which are the most probable chromophore.

The colored and uncolored samples of tugtupite differ only in the presence of an absorption band with a maximum in the region of 520 nm. Otherwise, the absorption spectra in the range of 300–2000 nm coincide. Thus, we can assume the following mechanism of photochromism in tugtupite: $S_4^{2-} + S_2^{\bullet-} \xrightarrow{h\nu=400\ nm} S_4^{\bullet-} + S_2^{2-} \xrightarrow{h\nu=500\ nm} S_4^{2-} + S_2^{\bullet-}$. No significant differences are found in the absorption spectra of colored and uncolored samples, since the absorption bands of $S_4^{\bullet-}$ are in the same spectral region as those of $S_2^{\bullet-}$ [93].

The bluish-violet color of meionite (Sample 16) is related with an absorption band with a maximum at 600 nm and vibrational repetitions at a distance of about 1100 cm^{-1}. A similar color was observed for $(CO_3)^{2-}$-bearing marialite after the irradiation by short-wave ultraviolet light [89]. According to our preliminary data, the ESR spectra of the bluish samples of the scapolite-group minerals contain a signal with g = 2.014. Earlier, similar spectra were observed for other blue minerals containing carbonate anion, namely, cancrinite [110,111] and CO_3^{2-}-bearing kyanoxalite [12]. In these minerals, the $(CO_3)^{\bullet-}$ radical anion is the main color center.

5. Conclusions

The application of a multimethodical approach involving various spectroscopic methods, as well as chemical and structural data, to feldspathoids belonging to the sodalite, cancrinite and scapolite groups made it possible to identify various S-bearing extra-framework anions, radical anions and neutral molecules. The complex mutual transformations of these components are observed during heating at high temperatures.

Based on these data and data on the synthesis of S-bearing feldspathoids under reducing and oxidizing conditions, it was confirmed that the composition of an extra-framework species in these minerals can be considered as a marker of mineral-forming media, including the fugacities of the volatile components (H_2O, O_2, CO_2, HF, SO_2 and polysulfide compounds).

The SO_4^{2-} anion and the $S_3^{\bullet-}$ radical anion are the most stable species at high temperatures under oxidizing conditions. Under reducing conditions, depending on the temperature and charge-balance requirement, these species transform into S^{2-}, HS^-, $S_4^{\bullet-}$, $S_2^{\bullet-}$ and/or S_4.

The S-bearing species $S_2^{\bullet-}$, $S_3^{\bullet-}$, $S_4^{\bullet-}$, S_4 and S_5^{2-}, as well as S_6 (in slyudyankaite), are the most common color centers in feldspathoids. The luminescence of these minerals under UV light is mainly due to the presence of $S_2^{\bullet-}$ and/or Fe^{3+}.

Author Contributions: Conceptualization, N.V.C., R.Y.S. and I.V.P.; methodology, N.V.C., N.V.S., R.Y.S., M.F.V., V.D.S. and D.A.V.; collecting of minerals, A.N.S., N.V.C. and I.V.P.; investigation, R.Y.S., N.V.C., V.L.T., S.V.L., M.F.V., V.D.S., I.V.P., D.A.V., A.V.K. and N.V.Z.; original manuscript draft preparation, N.V.C., A.N.S., R.Y.S., N.V.S. and V.L.T.; manuscript review and editing, N.V.C., R.Y.S., I.V.P., N.V.S. and D.A.V.; figures, N.V.C., R.Y.S., N.V.S. and S.V.L. All authors have read and agreed to the published version of the manuscript.

Funding: All spectroscopic studies and synthesis, as well as data generalization and theoretical analysis were supported by the Russian Science Foundation, grant No. 22-17-00006, https://rscf.ru/project/22-17-00006/ (accessed on 17 November 2022) (for N.V.C., I.V.P., R.Yu.S., N.V.S., N.V.Z., V.D.S. and M.F.V.). Collecting of minerals, their identification and chemical analyses were carried out in accordance with the state task, state registration No. AAA-A19-119092390076-7. The authors thank the laboratory of materials research of LUCH Research and production Association, Research and Development Institute (Podolsk, Russia) for X-ray powder diffraction analysis of synthetic compounds.

Data Availability Statement: Not applicable.

Conflicts of Interest: The authors declare no conflicts of interest.

References

1. Ballirano, P.; Maras, A.; Buseck, P.R. Crystal chemistry and IR spectroscopy of Cl- and SO_4-bearing cancrinite-like minerals. *Amer. Mineral*. **1996**, *81*, 1003–1012. https://doi.org/10.2138/am-1996-7-822.
2. Bonaccorsi, E.; Merlino, S. Modular microporous minerals: Cancrinite-davyne group and C-S-H phases, *Rev. Mineral. Geochem*. **2005**, *57*, 241–290. https://doi.org/10.2138/rmg.2005.57.8.
3. Merlino, S. Feldspathoids: Their average and real structures. In *Feldspars Feldspathoids*; Brown, W.L., Ed.; NATO ASI Series; Springer: Dordrecht, The Netherlands, 1984; Volume 137, pp. 435–470. https://doi.org/10.1007/978-94-015-6929-3_12.
4. Chukanov, N.V.; Aksenov, S.M.; Rastsvetaeva, R.K. Structural chemistry, IR spectroscopy, properties, and genesis of natural and synthetic microporous cancrinite- and sodalite-related materials: A review. *Micropor. Mesopor. Mater*. **2021**, *323*, 111098. https://doi.org/10.1016/j.micromeso.2021.111098.
5. Chukanov, N.V.; Sapozhnikov, A.N.; Shendrik, R.Y.; Vigasina, M.F.; Steudel, R. Spectroscopic and crystal-chemical features of sodalite-group minerals from gem lazurite deposits. *Minerals* **2020**, *10*, 1042. https://doi.org/10.3390/min10111042.
6. Sapozhnikov, A.N.; Tauson, V.L.; Lipko, S.V.; Shendrik, R.Y.; Levitskii, V.I.; Suvorova, L.F.; Chukanov, N.V.; Vigasina, M.F. On the crystal chemistry of sulfur-rich lazurite, ideally $Na_7Ca(Al_6Si_6O_{24})(SO_4)(S_3)^{-}{\cdot}nH_2O$. *Amer. Mineral*. **2021**, *106*, 226–234. https://doi.org/10.2138/am-2020-7317.
7. Chukanov, N.V.; Zubkova, N.V.; Pekov, I.V.; Shendrik, R.Y.; Varlamov, D.A.; Vigasina, M.F.; Belakovskiy, D.I.; Britvin, S.N.; Yapaskurt, V.O.; Pushcharovsky, D.Y. Sapozhnikovite, $Na_8(Al_6Si_6O_{24})(HS)_2$, a new sodalite-group mineral from the Lovozero alkaline massif, Kola Peninsula. *Mineral. Mag*. **2022**, *86*, 49–59. https://doi.org/10.1180/mgm.2021.94.
8. Chukanov, N.V.; Vigasina, M.F.; Zubkova, N.V.; Pekov, I.V.; Schäfer, C.; Kasatkin, A.V.; Yapaskurt, V.O.; Pushcharovsky, D.Y. Extra-framework content in sodalite-group minerals: Complexity and new aspects of its study using infrared and Raman spectroscopy. *Minerals* **2020**, *10*, 363. https://doi.org/10.3390/min10040363.
9. Chukanov, N.V.; Zubkova, N.V.; Varlamov, D.A.; Pekov, I.V.; Belakovskiy, D.I.; Britvin, S.N.; Van, K.V.V.; Ermolaeva, V.N.; Vozchikova, S.A.; Pushcharovsky, D.Y. Steudelite, $(Na_3)[(K,Na)_{17}Ca_7]Ca_4(Al_{24}Si_{24}O_{96})(SO_3)_6F_6{\cdot}4H_2O$, a new cancrinite-group mineral with afghanite-type framework topology. *Phys. Chem. Miner.* **2022**, *49*, 1. https://doi.org/10.1007/s00269-021-01172-4.
10. Chukanov, N.V.; Pekov, I.V.; Olysych, L.V.; Massa, W.; Zadov, A.E.; Rastsvetaeva, R.K.; Vigasina, M.F. Kyanoxalite, a new cancrinite-group mineral species with extraframework oxalate anion from the Lovozero alkaline pluton, Kola peninsula. *Geol. Ore. Depos*. **2010**, *52*, 778–790. https://doi.org/10.1134/S107570151008009X.
11. Olysych, L.V.; Vigasina, M.F.; Melchakova, L.V.; Pekov, I.V.; Chukanov, N.V. Study of thermal decomposition of the cancrinite-kyanoxalite solid-solution series minerals. In Proceedings of the Abstracts of the XXVII International Conference "Geochemistry of Magmatic Rocks", school "Geochemistry of Alkaline Rocks", Moscow-Koktebel, Russia-Ukraine, September 9–16, **2010**, 135–136.
12. Chukanov, N.V.; Vigasina, M.F.; Shendrik, R.Y.; Varlamov, D.A.; Pekov, I.V.; Zubkova, N.V. Nature and isomorphism of extra-framework components in cancrinite- and sodalite-related minerals: New data. *Minerals* **2022**, *12*, 729. https://doi.org/10.3390/min12060729.
13. Chukanov, N.V.; Shendrik, R.Y.; Vigasina, M.F.; Pekov, I.V.; Sapozhnikov, A.N.; Shcherbakov, V.D.; Varlamov, D.A. Crystal chemistry, isomorphism, and thermal conversions of extra-framework components in sodalite-group minerals. *Minerals* **2022**, *12*, 887. https://doi.org/10.3390/min12070887.
14. Shchipalkina, N.V.; Pekov, I.V.; Koshlyakova, N.N.; Britvin, S.N.; Zubkova, N.V.; Varlamov, D.A.; Sidorov, E.G. Unusual silicate mineralization in fumarolic sublimates of the Tolbachik volcano, Kamchatka, Russia—Part 2: Tectosilicates. *Eur. J. Mineral*. **2020**, *32*, 121–136. https://doi.org/10.5194/ejm-32-121-2020.
15. Lo Giudice, A.; Angelici, D.; Re, A.; Gariani, G.; Borghi, A.; Calusi, S.; Giuntini, L.; Massi, M.; Castelli, L.; Taccetti, F.; et al. Protocol for lapis lazuli provenance determination: Evidence for an Afghan origin of the stones used for ancient carved artefacts kept at the Egyptian Museum of Florence (Italy). *Archaeol. Anthropol. Sci.* **2017**, *9*, 637–651. https://doi.org/10.1007/s12520-016-0430-0.
16. Tauson, V.L.; Sapozhnikov, A.N.; Shinkareva, S.N.; Lustenberg, E.E. Indicative properties of lazurite as a member of clathrasil mineral family. *Dokl. Earth Sci.* **2011**, *441*, 1732–1737. https://doi.org/10.1134/S1028334X11120312.
17. Gobeltz-Hautecoeur, N.; Demortier, A.; Lede, B.; Lelieur, J.P.; Duhayon, C. Occupancy of the sodalite cages in the blue ultramarine pigments. *Inorg. Chem*. **2002**, *41*, 2848–2854. https://doi.org/10.1021/ic010822c.
18. Heil, C.; Cataldo, S.; Bachelet, G.B.; Boeri, L. Superconductivity in sodalite-like yttrium hydride clathrates. *Phys. Rev. B Condens. Matter*. **2019**, *99*, 220502(R). https://doi.org/10.1103/PhysRevB.99.220502.
19. Ogura, M.; Morozumi, K.; Elangovan, S.P.; Tanada, H.; Ando, H.; Okubo, T. Potassium-doped sodalite: A tectoaluminosilicate for the catalytic material towards continuous combustion of carbonaceous matters. *Appl. Catal. B*. **2008**, *77*, 294–299. https://doi.org/10.1016/j.apcatb.2007.07.033.
20. Shanbhag, G.V.; Choi, M.; Kim, J.; Ryoo, R. Mesoporous sodalite: A novel, stable solid catalyst for base-catalyzed organic transformations. *J. Catal*. **2009**, *264*, 88–92. https://doi.org/10.1016/j.jcat.2009.03.014.

21. Sachse, A.; Galarneau, A.; Renzo, F.D.; Fajula, F.; Coq, B. Synthesis of zeolite monoliths for flow continuous processes. The case of sodalite as a basic catalyst. *Chem. Mater*. **2010**, *22*, 4123–4125. https://doi.org/10.1021/cm1014064.
22. Hiyoshi, N. Nanocrystalline sodalite: Preparation and application to epoxidation of 2-cyclohexen-1-one with hydrogen peroxide. *Appl. Catal*. **2012**, *A419–A420*, 164–169. https://doi.org/10.1016/j.apcata.2012.01.026.
23. Manique, M.C.; Lacerda, L.V.; Alves, A.K.; Bergmann, C.P. Biodiesel production using coal fly ash-derived sodalite as a heterogeneous catalyst. *Fuel* **2017**, *190*, 268–273. https://doi.org/10.1016/j.fuel.2016.11.016.
24. Wang, S.; Zhao, Z.-J.; Chang, X.; Zhao, J.; Tian, H.; Yang, C.; Li, M.; Fu, Q.; Mu, R.; Gong, J. Activation and spillover of hydrogen on sub-1 nm palladium nanoclusters confined within sodalite zeolite for the semi-hydrogenation of alkynes. *Angew. Chem. Int. Ed*. **2019**, *58*, 7668–7672. https://doi.org/10.1002/anie.201903827.
25. Khajavi, S.; Jansen, J.C.; Kapteijn, F. Production of ultra pure water by desalination of seawater using a hydroxyl sodalite membrane. *J. Membr. Sci*. **2010**, *356*, 52–57. https://doi.org/10.1016/j.memsci.2010.03.026.
26. Nabavi, M.S.; Mohammadi, T.; Kazemimoghadam, M. Hydrothermal synthesis of hydroxyl sodalite zeolite membrane: Separation of H_2/CH_4. *Ceram. Int*. **2014**, *40*, 5889–5896. https://doi.org/10.1016/j.ceramint.2013.11.033.
27. Kalantari, N.; Vaezi, M.J.; Yadollahi, M.; Babaluo, A.A.; Bayati, B.; Kazemzadeh, A. Synthesis of nanostructure hydroxysodalite composite membranes via hydrothermal method: Support surface modification and synthesis method effects. *Asia Pac. J. Chem. Eng*. **2015**, *10*, 45–55. https://doi.org/10.1002/apj.1844.
28. Wei, X.-L.; Pan, W.-Y.; Li, X.; Pan, M.; Huo, C.-F.; Yang, R.; Chao, Z.-S. MCM-22 zeolite-induced synthesis of thin sodalite zeolite membranes. *Chem. Mater*. **2020**, *32*, 333–340. https://doi.org/10.1021/acs.chemmater.9b03845.
29. Yang, G.; Guo, H.; Kang, Z.; Feng, S.; Zhao, L.; Mintova, S. Sandwich-type H_2/CO_2 membranes comprising of graphene oxide and sodalite crystals with adjustable morphology and size. *Micropor. Mesopor. Mater*. **2020**, *300*, 110120. https://doi.org/10.1016/j.micromeso.2020.110120.
30. Eterigho-Ikelegbe, O.; Bada, S.O.; Daramola, M.O. Preparation and evaluation of nanocomposite sodalite/α-Al_2O_3 tubular membranes for H_2/CO_2 separation, *Membranes* **2020**, *10*, 312. https://doi.org/10.3390/membranes10110312.
31. Eden, C.L.; Daramola, M.O. Evaluation of silica sodalite infused polysulfone mixed matrix membranes during H_2/CO_2 separation. *Mater. Today Proc.* **2021**, *38*, 522–527. https://doi.org/10.1016/j.matpr.2020.02.393.
32. Ntshangase, N.C.; Sadare, O.O.; Daramola, M.O. Effect of silica sodalite functionalization and PVA coating on performance of sodalite infused PSF membrane during treatment of acid mine drainage. *Membranes* **2021**, *11*, 315. https://doi.org/10.3390/membranes11050315.
33. Navarro, J.A.R.; Barea, E.; Salas, J.M.; Masciocchi, N.; Galli, S.; Sironi, A.; Ania, C.O.; Parra, J.P. H_2, N_2, CO, and CO_2 sorption properties of a series of robust sodalite-type microporous coordination polymers. *Inorg. Chem*. **2006**, *45*, 2397–2399. https://doi.org/10.1021/ic060049r.
34. Asgari, A.; Jawahery, S.; Bloch, E.D.; Hudson, M.R.; Flacau, R.; Vlaisavljevich, B.; Long, J.R.; Brown, C.M.; Queen, W.L. An experimental and computational study of CO_2 adsorption in the sodalite-type *M*-BTT (*M* = Cr, Mn, Fe, Cu) metal–organic frameworks featuring open metal sites. *Chem. Sci*. **2018**, *9*, 4579–4588. https://doi.org/10.1039/C8SC00971F.
35. Wang, Y.; Jiang, Y.; Hu, S.; Peng, S.; Xu, C.; Lu, A. Dehydrated $Na_6[AlSiO_4]_6$ sodalite as a promising SO_2 sorbent material: A first principles thermodynamics prediction., *J. Amer. Ceram. Soc*. **2019**, *102*, 3663–3672. https://doi.org/10.1111/jace.16223.
36. Asgari, M.; Semino, R.; Schouwink, P.A.; Kochetygov, I.; Tarver, J. Understanding how ligand functionalization influences CO_2 and N_2 adsorption in a sodalite metal-organic framework. *Chem. Mater*. **2020**, *32*, 1526–1536. https://doi.org/10.1021/acs.chemmater.9b04631.
37. Dickson, J.O.; Harsh, J.B.; Lukens, W.W.; Pierce, E.M. Perrhenate incorporation into binary mixed sodalites: The role of anion size and implications for technetium-99 sequestration. *Chem. Geol*. **2015**, *395*, 138–143. https://doi.org/10.1016/j.chemgeo.2014.12.009.
38. Gilbert, M.R. Pressureless sintering of sodalite waste-forms for the immobilization of pyroprocessing wastes. *MRS Online Proc. Libr*. **2014**, *1744*, 61–66. https://doi.org/10.1557/opl.2015.394.
39. Luksic, S.A.; Riley, B.J.; Parker, K.E.; Hrma, P. Sodalite as a vehicle to increase Re retention in waste glass stimulant during vitrification. *J. Nucl. Mater*. **2016**, *479*, 331–337. https://doi.org/10.1016/j.jnucmat.2016.07.002.
40. Vance, E.R.; Gregg, D.J.; Grant, C.; Stopic, A.; Maddrell, E.R. Silver iodide sodalite for ^{129}I immobilization. *J. Nucl. Mater*. **2016**, *480*, 177–181. https://doi.org/10.1016/j.jnucmat.2016.08.013.
41. Lilova, K.; Pierce, E.M.; Wu, L.; Jubb, A.M.; Subramani, T.; Navrotsky, A. Energetics of salt-bearing sodalites, $Na_8Al_6Si_6O_{24}X_2$ (*X* = SO_4, ReO_4, Cl, I): A treatment option for pertechnetate-enriched nuclear waste streams. *ACS Earth Space Chem*. **2020**, *4*, 2153–2161. https://doi.org/10.1021/acsearthspacechem.0c00244.
42. Grajciar, L. PbS clusters embedded in sodalite zeolite cavities of different compositions: Unraveling the structural evolution and optical properties using ab initio calculations. *J. Phys. Chem*. **2016**, *C120*, 27050–27065. https://doi.org/10.1021/acs.jpcc.6b09423.
43. Van den Berg, A.W.C.; Bromley, S.T.; Jansen, J.C. Thermodynamic limits on hydrogen storage in sodalite framework materials: A molecular mechanics investigation. *Micropor. Mesopor. Mater*. **2005**, *78*, 63–71. https://doi.org/10.1016/j.micromeso.2004.09.017.
44. Zheng, Z.; Guliants, V.V.; Misture, S. Sodalites as ultramicroporous frameworks for hydrogen separation at elevated temperatures: Thermal stability, template removal, and hydrogen accessibility. *J. Porous Mater*. **2009**, *16*, 343–347. https://doi.org/10.1007/s10934-008-9206-y.

45. Rüscher, C.H.; Stemme, F.; Schomborg, L.; Buhl, J.-C. Low temperature hydrogen release from borontetrahydride-sodalite and its reloading: Observations in *in-situ* and *ex-situ* TIR experiments. In *Ceramics for Environmental and Energy Applications*; Boccaccini, A., Marra, J., Dogan, F., Lin, H.-T., Watanabe, T., Eds.; Wiley: Hoboken, NJ, USA, 2010; pp. 65–70.
46. Gong, Y.-N.; Meng, M.; Zhong, D.-C.; Huang, Y.-L.; Jiang, L.; Lu, T.-B. Counter-cation modulation of hydrogen and methane storage in a sodalite-type porous metal–organic framework. *Chem. Commun*. **2012**, *48*, 12002–12004. https://doi.org/10.1039/C2CC35461F.
47. Rejmak, P. Computational refinement of the puzzling red tetrasulfur chromophore in ultramarine pigments. *Phys. Chem. Chem. Phys*. **2020**, *22*, 22684–22698. https://doi.org/10.1039/D0CP03019H.
48. Eckert, B.; Steudel, F. Molecular spectra of sulfur molecules and solid sulfur allotropes. *Top. Curr. Chem.* **2003**, *231*, 31–97. https://doi.org/10.1007/b13181.
49. Hettmann, K.; Wenzel, T.; Marks, M.; Markl, G. The sulfur speciation in S-bearing minerals: New constraints by a combination of electron microprobe analysis and DFT calculations with special reference to sodalite-group minerals. *Amer. Mineral.* **2012**, *97*, 1653–1661.
50. Steudel, R. Inorganic polysulfides S_n^{2-} and radical anions $S_n^{\bullet-}$. In *Elemental Sulfur und Sulfur-Rich Compounds II. Topics in Current Chemistry*; Steudel, R., Ed.; Springer: Berlin/Heidelberg, Germany, 2003; Volume 231.
51. Chivers, T.; Elder, P.J.W. Ubiquitous trisulfur radical anion: fundamentals and applications in materials science, electrochemistry, analytical chemistry and geochemistry. *Chem. Soc. Rev.* **2013**, *42*, 5996–6005. https://doi.org/10.1039/c3cs60119f
52. Wong, M.W.; Steudel, R. Structure and spectra of tetrasulfur S_4—An ab initio MO study. *Chem. Phys. Lett.* **2003**, *379*, 162–169. https://doi.org/10.1016/j.cplett.2003.08.026.
53. Caggiani, M.C.; Mangone, A.; Aquafredda, P. Blue coloured haüyne from Mt. Vulture (Italy) volcanic rocks: SEM-EDS and Raman investigation of natural and heated crystals. *J. Raman Spectrosc*. **2022**, *53*, 956–968. https://doi.org/10.1002/jrs.6310.
54. Bény, C.; Guilhaumou, N.; Touray, J.-C. Native-sulphur-bearing fluid inclusions in the CO_2-H_2S-H_2O-S system—Microthermometry and Raman microprobe (MOLE) analysis—Thermochemical interpretations. *Chem. Geol*. **1982**, *37*, 113–127.
55. Dubessy, J.; Boiron, M.-C.; Moissette, A.; Monnion, C.; Sretenskaya, N. Determination of water, hydrates and pH in fluid inclusions by micro-Raman spectrometry. *Eur. J. Mineral*. **1992**, *4*, 885–894.
56. Weser, G.; Hensel, F.; Warren, W.W. The optical absorption spectrum of fluid sulfur up to supercritical conditions. *Ber. Bunsenges. Phys. Chem.* **1978**, *82*, 588–594. https://doi.org/10.1002/bbpc.197800123.
57. Paniz, H.; Lester, A. Vibronic absorption spectra of S_3 and S_4, in solid argon. *J. Phys. Chem.* **1992**, *96*, 6579–6585.
58. Steudel, R.; Jensen, D.; Göbel, P.; Hugo, P. Optical absorption spectra of the homocyclic sulfur molecules S_n (n = 6, 7, 8, 9, 10, 12, 15, 20) in solution. *Ber. Bunsenges. Phys. Chem*. **1988**, *92*, 118–122.
59. Raulin, K.; Gobeltz, N.; Vezin, H.; Touat, N.; Ledé, B.; Moissette, A. Identification of the EPR signal of S_2^- in green ultramarine pigments. *Phys. Chem. Chem. Phys*. **2011**, *13*, 9253–9259.
60. Ostroumov, M.; Fritsch, E.; Faulques, E.; Chauvet, O. Etude spectrometrique de la lazurite du Pamir, Tajikistan. Canad. Mineral. **2002**, *40*, 885–893. https://doi.org/10.2113/gscanmin.40.3.885.
61. Huie, R.E.; Clifton, C.L.; Altstein, N. A pulse radiolysis and flash photolysis study of the radicals SO_2^-, SO_3^-, SO_4^- and SO_5^-. *Int. J. Radiat. Appl. Instr. Part C Radiat. Phys. Chem*. **1989**, *33*, 361–370. https://doi.org/10.1016/1359-019790034-9.
62. McElroy, W.J.; Waygood, S.J. Kinetics of the reactions of the SO_4^- radical with SO_4^-, $S_2O_8^{2-}$, H_2O and Fe^{2+}. *J. Chem. Soc. Faraday Trans.* **1990**, *86*, 2557. https://doi.org/10.1039/FT9908602557.
63. Steudel, R.; Chivers, T. The role of polysulfide dianions and radical anions in the chemical, physical and biological sciences, including sulfur-based batteries. *Chem. Soc. Rev.* **2019**, *48*, 3279–3319 and 4338.
64. Olysych, L.V. Structural and Genetic Mineralogy of the Cancrinite Group in Intrusive Alkaline Complexes. Ph.D. Thesis, Lomonosov Moscow State University, Moscow, Russia, 2010; 307p. (In Russian)
65. Sapozhnikov, A.N.; Kaneva, E.V.; Cherepanov, D.I.; Suvorova, L.F.; Levitsky, V.I.; Ivanova, L.A.; Reznitsky, L.Z. Vladimirivanovite, $Na_6Ca_2[Al_6Si_6O_{24}](SO_4,S_3,S_2,Cl)_2{\cdot}H_2O$, a new mineral of sodalite group. *Geol. Ore Depos*. **2012**, *54*, 557–564. https://doi.org/10.1134/S1075701512070070.
66. Zubkova, N.V.; Chukanov, N.V.; Varlamov, D.A.; Vigasina, M.F.; Pekov, I.V.; Ksenofontov, D.A.; Pushcharovsky, D.Y. SO_3^{2-}-bearing analogue of marinellite: Crystal structure and vibrational spectroscopy. *Geol. Ore Depos*. **2022**, *in press*.
67. Chukanov, N.V.; Rastsvetaeva, R.K.; Pekov, I.V.; Zadov, A.E.; Allori, R.; Zubkova, N.V.; Giester, G.; Pushcharovsky, D.Y.; Van, K.V. Biachellaite, $(Na,Ca,K)_8(Si_6Al_6O_{24})(SO_4)_2(OH)_{0.5}{\cdot}H_2O$, a new mineral species of the cancrinite group. *Geol. Ore Depos*. **2009**, *51*, 588–594. https://doi.org/10.1134/S1075701509070071.
68. Tauson, V.L.; Goettlicher, J.; Sapozhnikov, A.N.; Mangold, S.; Lustenberg, E.E. Sulfur speciation in lazurite-type minerals $(Na,Ca)_8[Al_6Si_6O_{24}](SO_4,S)_2$ and their annealing products: A comparative XPS and XAS study. *Eur. J. Mineral*. **2012**, *24*, 133–152.
69. Chukanov, N.V.; Pekov, I.V.; Olysych, L.V.; Zubkova, N.V.; Vigasina, M.F. Crystal chemistry of cancrinite-group minerals with AB-type frameworks. II. IR spectroscopy and its crystal chemical implications: Review and new data. *Canad. Mineral*. **2011**, *49*, 1151–1164. https://doi.org/10.3749/canmin.49.5.1151.
70. Pekov, I.V.; Olysych, L.V.; Chukanov, N.V.; Zubkova, N.V.; Pushcharovsky, D.Y.; Van, K.V.; Giester, G.; Tillmanns, E. Crystal chemistry of cancrinite-group minerals with AB-type frameworks. I. Chemical and structural variations: Review and new data. *Canad. Mineral*. **2011**, *49*, 1129–1150. https://doi.org/10.3749/canmin.49.5.1129.

71. Frost, R.L.; Keeffe, E.C. Raman spectroscopic study of the sulfite-bearing minerals scotlandite, hannebachite and orschallite: Implications for the desulfation of soils. *J. Raman Spectrosc*. **2009**, *40*, 244–248.
72. Sapozhnikov, A.N.; Ivanov, V.G.; Piskunova, L.F.; Kashaev, A.A.; Terentieva, E.A.; Pobedimskaya, L.E. Bystrite $Ca(Na,K)_7(Si_6Al_6O_{24})(S_3)_{1.5}\cdot 2H_2O$—A new cancrinite-like mineral. *Zap. Vsesyuznogo Miner. Obs.* **1991**, *120*, 97–100. (In Russian)
73. Sapozhnikov, A.N.; Kaneva, E.V.; Suvorova, L.F.; Levitsky, V.I.; Ivanova, L.A. Sulfhydrylbystrite, $Na_5K_2Ca(Al_6Si_6O_{24})(S_5)(SH)$, a new mineral with the LOS framework, and re-interpretation of bystrite: Cancrinite-group minerals with novel extra-framework anions, *Mineral. Mag*. **2017**, *81*, 383–402. https://doi.org/10.1180/minmag.2016.080.106.
74. Pobedimskaya, E.A.; Terentieva, L.E.; Sapozhnikov, A.N.; Kashaev, A.A.; Dorokhova, G.I. Crystal structure of bystrite. *Doklady Akad. Nauk SSSR*. **1991**, *319*, 873–878. (In Russian)
75. Chukanov, N.V. *Infrared Spectra of Mineral Species: Extended Library*; Springer: Dordrecht, The Netherlands; Heidelberg, Germany; New York, NY, USA; London, UK, 2014; 1716p.; ISBN 9400771274.
76. Chukanov, N.V.; Vigasina, M.F.; Rastsvetaeva, R.K.; Aksenov, S.M.; Mikhailova, J.A.; Pekov, I.V. The evidence of hydrated proton in eudialyte-group minerals based on Raman spectroscopy data. *J. Raman Spectrosc*. **2022**, *53*, 1188–1203. https://doi.org/10.1002/jrs.6343.
77. Van Doorn, C.Z.; Schipper, D.J. Luminescence of O^{2-}, Mn^{2+} and Fe^{3+} in sodalite. *Phys. Lett. A* **1971**, *34*, 139–140. https://doi.org/10.1016/0375-960190792-4.
78. Rastsvetaeva, R.K.; Sapozhnikov, A.N.; Tauson, V.L.; Kashaev, A.A. Crystal structure of sulfide sodalite, a product of sulfate sulfur reduction in lazurite. *Doklady Academii Nauk*. **1997**, *356*, 773–776 (In Russian)
79. Epelbaum, M.B.; Gorbatyi, Y.E.; Gusiynin, V.F.; Ivanov, I.P. Study of sodium sodalities with different intra-framework anions. In *Essays in Physicochemical Petrology*; Nauka: Moscow, Russia, 1970; Volume 2, pp. 269–280 (In Russian)
80. Tauson, V.L.; Akimov, V.V.; Sapozhnikov, A.N.; Kuznetzov, K.E. Investigation of the stability conditions and structural-chemical transformations of Baikal lazurite. *Geochemi. Int.* **1998**, *36*, 717–733.
81. Sapozhnikov, A.N.; Tauson, V.L.; Matveeva, L.N. Stepwise change of modulation wavelength in structure of cubic lazurite under annealing. *Zap. Ross. Mineral. Obs. Proc. Rus. Mineral. Soc.* **2001**, *2*, 121–125. (In Russian)
82. Urusov, V.S. *Theory of Isomorphic Miscibility*; Nauka: Moscow, Russia, 1977; 251p. (In Russian)
83. Urusov, V.S. The problem of the dimension parameter in the isomorphism theory and effective radii of aluminosilicate radicals. *Mineral. Zhurnal* **1980**, *2*, 3–11 (In Russian)
84. Urusov, V.S. Crystal chemical and energetic characterization of solid solution. In *Advances in Physical Geochemistry X. Thermodynamic Data: Systematics and Estimation*; Saxena, S.K., Ed.; Springer: New York, NY, USA, 1992; Volume 10, pp. 162–194.
85. Kotel'nikov, A.R.; Koval'skiy, A.M.; Suk, M.I. Experimental investigation of sodalite solid solutions with anionic isomorphism of chlorine and sulfur. *Geokhimiya* **2005**, *34*, 599–613. (In Russian)
86. Gaft, M.; Panczer, G.; Nagli, L.; Yeates, H. Laser-induced time-resolved luminescence of tugtupite, sodalite and hackmanite. *Phys. Chem. Miner.* **2008**, *36*, 127–141. https://doi.org/10.1007/s00269-008-0263-1.
87. Radomskaya, T.A.; Kaneva, E.V.; Shendrik, R.Y.; Suvorova, L.F.; Vladykin, N.V. Sulfur-bearing sodalite, hackmanite, in alkaline pegmatites of the Inagli massif (Aldan Shield): Crystal chemistry, photochromism, and luminescence. *Geol. Ore Depos*. **2021**, *63*, 696–704.
88. Blumentritt, F.; Fritsch, E. Photochromism and photochromic gems: A review and some new data (Part 1). *J. Gemmol.* **2021**, *37*, 780–800. https://doi.org/10.15506/JoG.2021.37.8.780.
89. Agamah, C.; Vuori, S.; Colinet, P.; Norrbo, I.; Miranda de Carvalho, J.; Key, L.; Nakamura, O.; Lindblom, J.; van Goethem, L.; Emmermann, A. Hackmanite—The natural glow-in-the-dark material. *Chem. Mater*. **2020**, *32*, 8895–8905.
90. Jensen, A.; Petersen, O.V. Tugtupite: A gemstone from Greenland. *Gems Gemol*. **1982**, *18*, 90–94.
91. Warner, T.E.; Hutzen Andersen, J. The effects of sulfur intercalation on the optical properties of artificial "hackmanite", $Na_8[Al_6Si_6O_{24}]Cl_{1.8}S_{0.1}$; "sulfosodalite", $Na_8[Al_6Si_6O_{24}]s$; and natural tugtupite, $Na_8[Be_2Al_2Si_8O_{24}](Cl,S)_{2-\delta}$. *Phys. Chem, Miner*. **2011**, *39*, 163–168. https://doi.org/10.1007/s00269-011-0471-y.
92. Arieli, D.; Vaughan, D.E.W.; Goldfarb, D. New synthesis and insight into the structure of blue ultramarine pigments. *J. Amer. Chem. Soc*. **2004**, *126*, 5776–5788. https://doi.org/10.1021/ja0320121.
93. Tossell, J.A. Calculation of the visible-UV absorption spectra of hydrogen sulfide, bisulfide, polysulfides, and As and Sb sulfides, in aqueous solution. *Geochem. Trans*. **2003**, *4*, 28. https://doi.org/10.1039/b305086f.
94. Vannotti, L.E.; Morton, J.R. Paramagnetic-resonance spectra of S_2^- in alkali halides. *Phys. Rev*. **1967**, *161*, 282–286. https://doi.org/10.1103/PhysRev.161.282.
95. Chukanov, N.V.; Vigasina, M.F. *Vibrational (Infrared and Raman) Spectra of Minerals and Related Compounds*; Springer: Dordrecht, The Netherlands, 2020; 1376p. https://doi.org/10.1007/978-3-030-26803-9.
96. Hassan, I.; Grundy, H.D. The crystal structures of sodalite-group minerals. *Acta Cryst*. **1984**, *B40*, 6–13. https://doi.org/10.1107/S0108768184001683.
97. Hassan, I.; Buseck, P. Cluster ordering and antiphase domain boundaries in haüyne. *Can. Miner*. **1989**, *27*, 173–180.
98. Meuwsen, A.; Heinze, G. Darstellung einiger Schwermetall-Trithionate. *Z. Anorg. Allgem. Chem*. **1952**, *69*, 86–91. (In German)
99. Gabelica, Z. Compounds containing cadmium and thiosulfate ions. X. Infrared and Raman investigation of the structural behavior of the $S_2O_3^{2-}$ ion in cadmium thiosulfate dihydrate, $CdS_2O_3\cdot 2H_2O$. *Chem. Lett*. **1979**, *8*, 1419–1422.
100. Gabelica, Z. Structural study of solid inorganic thiosulfates by infrared and Raman spectroscopy. *J. Molec. Struct*. **1980**, *60*, 131–138.

101. Matulionyte, J.; Ragauskas, R.; Eicher-Lorka, O.; Niaura, G. Raman spectroscopic study of anion-exchange membranes in modified photographic fixer solution. *Chemija* **2006**, *17*, 1–6.
102. Lindner, G.-G.; Massa, W.; Reinen, D. Structure properties of hydrothermally synthesized thiosulfate cancrinite. *J. Solid State Chem.* **1995**, *117*, 386–391.
103. Bindi, L.; Nestola, F.; Kolitsch, U.; Guastoni, A.; Zorzi, F. Fassinaite, $Pb_2^{2+}(S_2O_3)(CO_3)$, the first mineral with coexisting thiosulphate and carbonate groups: Description and crystal structure. *Mineral. Mag.* **2011**, *75*, 2721–2732.
104. Chukanov, N.V.; Zubkova, N.V.; Pekov, I.V.; Giester, G.; Pushcharovsky, D.Y. Sulfite analogue of alloriite from Sacrofano, Latium, Italy: Crystal chemistry and specific features of genesis. *Geol. Ore Depos.* **2021**, *63*, 793–804. https://doi.org/10.1134/S1075701521080043.
105. Hassan, I.; Grundy, H.D. The structure of nosean, ideally $Na_8[Al_6Si_6O_{24}]SO_4{\cdot}H_2O$. *Canad. Mineral.* **1989**, *27*, 165–172.
106. Hassan, I.; Grundy, H.D. The crystal structure of haüyne at 294 and 153 K. *Canad. Mineral.* **1991**, *29*, 123–130.
107. Sapozhnikov, A.N.; Bolotina, N.B.; Chukanov, N.V.; Shendrik, R.Y.; Kaneva, E.V.; Vigasina, M.F.; Ivanova, L.A. Slyudyankaite, $Na_{28}Ca_4(Si_{24}Al_{24}O_{96})(SO_4)_6(S_6)_{1/3}(CO_2){\cdot}2H_2O$, a new sodalite-group mineral from the Malo-Bystrinskoe lazurite deposit, Baikal Lake area. *Amer. Mineral.* **2023**, *in press*.
108. Ivanov, V.G.; Sapozhnikov, A.N. *Lazurites of the USSR*; Nauka: Novosibirsk, Russia, 1985; 172p. (In Russian)
109. Bolotina, N.B.; Rastsvetaeva, R.K.; Sapozhnikov, A.N. Average structure of incommensurately modulated monoclinic lazurite. *Crystallogr. Rep.* **2006**, *51*, 589–595. https://doi.org/10.1134/S1063774506040080.
110. Shendrik, R.; Kaneva, E.; Radomskaya, T.; Sharygin, I.; Marfin, A. Relationships between the structural, vibrational, and optical properties of microporous cancrinite. *Crystals* **2021**, *11*, 280. https://doi.org/10.3390/cryst11030280.
111. Kaneva, E.; Shendrik, R. Radiation defects and intrinsic luminescence of cancrinite. *J. Lumin.* **2022**, *243*, 118628. https://doi.org/10.1016/j.jlumin.2021.118628.